INTERNATIONAL JOURNAL FOR NUMERICAL METHODS IN ENGINEERING
Int. J. Numer. Meth. Engng 2010; **84**:179–213
Published online 29 March 2010 in Wiley Online Library (wileyonlinelibrary.com). DOI: 10.1002/nme.2891

Coupling BEM/TBEM and MFS for the simulation of transient conduction heat transfer

António Tadeu, Nuno Simões and Inês Simões*, †

CICC, Department of Civil Engineering, University of Coimbra, 3030 Coimbra, Portugal

SUMMARY

The coupling between the boundary element method (BEM)/the traction boundary element method (TBEM) and the method of fundamental solutions (MFS) is proposed for the transient analysis of conduction heat transfer in the presence of inclusions, thereby overcoming the limitations posed by each method. The full domain is divided into sub-domains, which are modeled using the BEM/TBEM and the MFS, and the coupling of the sub-domains is achieved by imposing the required boundary conditions.

The accuracy of the proposed algorithms, using different combinations of BEM/TBEM and MFS formulations, is checked by comparing the resulting solutions against referenced solutions.

The applicability of the proposed methodology is shown by simulating the thermal behavior of a solid ring incorporating a crack or a thin inclusion in its wall. The crack is assumed to have null thickness and does not allow diffusion of energy; hence, the heat fluxes are null along its boundary. The thin inclusion is modeled as filled with thermal insulating material. Copyright © 2010 John Wiley & Sons, Ltd.

Received 22 June 2009; Revised 20 January 2010; Accepted 23 January 2010

KEY WORDS: BEM; TBEM; MFS; coupling; transient heat diffusion

1. INTRODUCTION

The heat diffusion field generated by the release of thermal energy from transient sources, such as those detected by the infrared thermography technique, has been studied in the past few decades. This interest has been growing since heat diffusion patterns can be used to detect cracks, voids and other classes of defects in materials and construction elements [1–5]. Several numerical simulation techniques have been proposed to improve our understanding of how heat waves propagate in solid and fluid media.

*Correspondence to: Inês Simões, CICC, Department of Civil Engineering, University of Coimbra, 3030 Coimbra, Portugal.
†E-mail: mivsimoes@itecons.uc.pt

Contract/grant sponsor: Portuguese Foundation for Science and Technology (FCT); contract/grant number: SFRH/BD/48138/2008

Copyright © 2010 John Wiley & Sons, Ltd.

Most of the models devised to solve transient diffusion heat problems are formulated in the time domain (time-marching), using Laplace transforms or frequency transforms. After Chang *et al.* [6], who were the first to apply a time-domain direct boundary integral method to study planar transient heat conduction, several authors employed boundary integral approaches, based on how the temperature and the flux values at each time step are obtained directly in the time domain [7–10]. An alternative to time marching is to transform the time domain. Since Rizzo and Shippy [11] proposed the boundary integral representation for transient heat conduction analysis, based on the Laplace transform, other authors have published different solutions for diffusion-type problems using Laplace transforms such as those presented by Cheng *et al.* [12] and Zhu *et al.* [13, 14]. More recently, Sutradhar *et al.* [15] used a Laplace transform boundary element method (BEM) approach to solve the 3D transient heat conduction in functionally graded materials, with thermal conductivity and heat capacitance varying exponentially in one coordinate. With the Laplace transform technique, a numerical transform inversion is required to calculate the physical variables in the real space after the solution has been obtained for a sequence of values of the transformed parameter. To overcome the accuracy loss in the inversion process, which magnifies small truncation errors, Stehfest [16] has proposed a stable algorithm [14, 17].

This work concerns an approach in which a Fourier transform applied in the time domain deals with the time variable of the diffusion equation to establish a frequency domain technique; time solutions are obtained by using inverse Fourier transforms into time–space. The time-aliasing phenomenon is avoided by using complex frequencies to attenuate the response at the end of the time frame. This effect is later taken into account by re-scaling the response in the time domain [18–20]. The use of a Fourier transform allows the problem to be seen as a combination of harmonic heat sources elicited by different excitation frequencies. The problem is thus physically solved as a system subjected to the propagation of heat waves. The resulting problem can be computed efficiently because the responses decay quickly at higher frequencies. The results at frequency 0.0 Hz, the static response, can be easily computed since the argument of the functions is complex.

Among the tools used to analyze heat diffusion in the presence of solid and fluid layering and other complex systems are the thin layer method (TLM) [21], the finite differences method (FDM) and the BEM [22].

Analytical solutions are known for very simple geometric and material conditions such as homogeneous full spaces, half-spaces and circular cylindrical inclusions subjected to line or point heat sources of constant amplitude and infinite duration. Analytical solutions can also be derived for solving more complex systems such as layered media, walls and slabs [19, 20]. However, the resulting integral expressions require great computational effort. These known solutions are often used as yardsticks against which one can judge the correctness and the quality of semi-numerical and/or discrete implementations. They can also be used in conjunction with the BEM, as Green's functions, to solve problems in stratified media with buried inclusions, thereby avoiding the discretization of the layer interface boundaries.

The BEM is one of the best tools for modeling homogeneous unbounded systems since the far field boundary conditions are automatically satisfied, requiring only the discretization of the boundaries of the inclusions. Hohage and Sayas [23] have proposed a numerical solution of the heat diffusion problem using the BEM that uses the Laplace transform. Ma *et al.* [24] used the BEM to study the transient heat conduction in 3D solids with fiber inclusions. The work of Wang *et al.* [25] is another example of the application of the BEM where time convolution integrals are used to compute transient diffusion.

Copyright © 2010 John Wiley & Sons, Ltd.

DOI: 10.1002/nme

Although the BEM requires only boundary meshing it still needs prior knowledge of fundamental solutions, i.e. Green's functions, and it involves sophisticated mathematics. Its efficiency also depends on the correct resolution of the singular and hypersingular integrals. This leads all too often to an undesirably high computational cost.

It is also known that when the heterogeneity thickness tends toward zero, as in the case of delaminations, small imperfections, cracks or thin defects, the conventional direct BEM degenerates and is no longer a valid basis for a numerical calculation modeling [26]. A traction boundary element method (TBEM) formulation is frequently implemented to overcome this problem. The TBEM is suitable to solve wave propagation problems. Prosper [27] and Prosper and Kausel [28] used the TBEM to model the 2D scattering of waves by flat and horizontal empty cracks of zero thickness in elastic media. The appearance of hypersingular integrals is one of the difficulties posed by these formulations. Various attempts have been made to overcome this difficulty [29, 30]. Amado Mendes and Tadeu [31] solved the case of a 2D empty crack buried in an unbounded medium subjected to a 3D source. Tadeu *et al.* [32] subsequently proposed a combined (or dual) BEM/TBEM formulation to solve the case of fluid-filled thin inclusions placed in an unbounded medium.

In recent years, a different class of numerical techniques has become popular, the so-called meshless techniques that require neither domain nor boundary discretization [33–38]. The method of fundamental solutions (MFS) seems to be particularly effective for studying wave propagation, overcoming some of the mathematical complexity of the BEM and providing accurate solutions at substantially lower computational cost. Godinho *et al.* [39] studied the performance of the MFS for simulating the propagation of acoustic waves and heat conduction in the presence of circular geometries. They concluded that the method can be very efficient, performing even better than the BEM for this type of problem. Godinho *et al.* [40] also successfully employed the MFS to study acoustic and elastic wave propagation around thin structures using a domain decomposition technique. More recently, the MFS was used to simulate ground rotations along 2D topographical profiles under the incidence of elastic plane waves [41]. Several authors have proposed the use of enrichment functions to model torsion problems, including cracks [42]. But the MFS has its own disadvantageous and limitations in problems involving thin inclusions and inclusions with twisting boundaries [40].

This work describes the coupling of the BEM/TBEM and the MFS to overcome some of the limitations posed separately by each method. These coupling formulations are presented for the transient analysis of heat diffusion problems in the presence of null-thickness and thin inclusions. The full domain is divided into sub-domains, which are modeled using the BEM/TBEM and the MFS, and the sub-domains are coupled by imposing the required boundary conditions. The approach is implemented to solve 2D problems. Reference solutions are used to ascertain the accuracy of the proposed coupling algorithms.

The problem is defined in the next section, and then the BEM/TBEM and MFS heat diffusion coupling formulations are established for different inclusions buried in an unbounded medium. The coupling formulations are first verified against solutions obtained from analytical, BEM, TBEM and MFS formulations, used as reference solutions. Then a brief section describes how responses in the time domain are obtained by means of the fast inverse Fourier transformation. Finally, the applicability of the proposed method is shown by means of two numerical examples. In the first, the TBEM/MFS coupling algorithm is used to determine the heat distribution evolution generated by a heat source placed inside a steel-filled ring with a null-thickness crack in its concrete wall. In the second, the (combined BEM+TBEM)/MFS coupling algorithm computes the heat diffusion for the same system in the presence of a thin inclusion, filled with thermal insulating material and placed within the ring.

Copyright © 2010 John Wiley & Sons, Ltd.

DOI: 10.1002/nme

2. BOUNDARY INTEGRAL COUPLING FORMULATIONS

Consider two irregular two-dimensional cylindrical inclusions, 1 and 2, embedded in a spatially uniform solid medium (Medium 1) with thermal diffusivity K_1 (see Figure 1). Media 2 and 3, inside inclusions 1 and 2, exhibit thermal diffusivities K_2 and K_3, respectively. Thermal diffusivity K_m is defined by $k_m/(\rho_m c_m)$, where k_m is the thermal conductivity, ρ_m is the density and c_m is the specific heat of each Medium m. Consider further that this system is subjected to a line heat source placed at O (x_s, y_s).

The transient heat transfer by conduction in each homogeneous and isotropic medium can be described by the diffusion equation in Cartesian coordinates,

$$\left(\frac{\partial^2}{\partial x^2}+\frac{\partial^2}{\partial y^2}\right)\hat{T}=\frac{1}{K_m}\frac{\partial \hat{T}}{\partial \tau} \tag{1}$$

in which τ is time, $\hat{T}(\tau, x, y)$ is the temperature at a point (x, y) in the domain. The solution of this equation can be obtained in frequency domain after the application of a Fourier transform in the time domain, which leads to the following equation:

$$(\nabla^2+(k_{\alpha_m})^2)T(x, y, \omega)=0 \tag{2}$$

where $k_{\alpha_m}=\sqrt{-\mathrm{i}\omega/K_m}$, $\mathrm{i}=\sqrt{-1}$ and ω is the frequency.

In the frequency domain, the incident heat diffusion generated at (x, y) by a source placed in Medium 1 can be expressed by

$$t_{\mathrm{inc}}(x, y, \omega)=\frac{-\mathrm{i}A}{4k_1}H_0(k_{\alpha_1}r_1) \tag{3}$$

where the subscript inc represents the incident field, $r_1=\sqrt{(x-x_s)^2+(y-y_s)^2}$, A is the heat amplitude and $H_n(\ldots)$ correspond to second Hankel functions of order n.

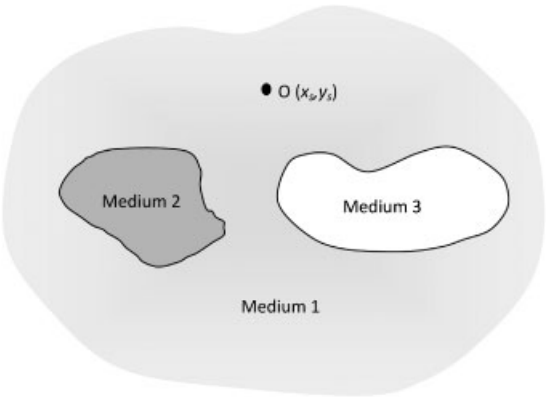

Figure 1. Sketch representing the geometry of the problem.

Copyright © 2010 John Wiley & Sons, Ltd.

DOI: 10.1002/nme

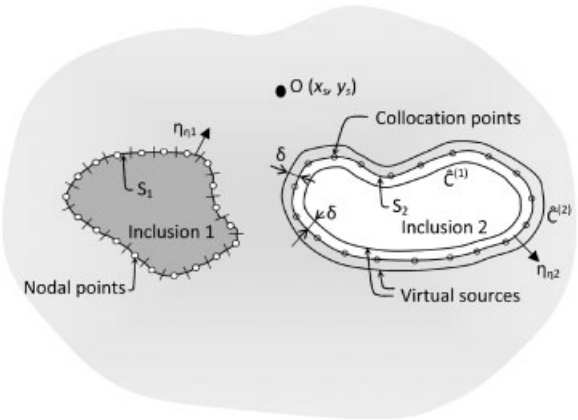

Figure 2. Scheme representing the discretization of inclusion 1 with boundary elements. Position of virtual heat sources and collocation points used to model inclusion 2.

2.1. BEM/MFS coupling formulation

This section describes how the coupling of the BEM and the MFS techniques is formulated to obtain the 2D heat diffusion field generated by a heat source. Inclusion 1 is modeled using the BEM technique, whereas inclusion 2 is modeled with the MFS. Three different boundary conditions may be ascribed to the inclusions' surfaces: continuity of temperatures and heat fluxes, null heat fluxes and null temperatures.

2.1.1. Continuity of temperatures and heat flux conditions along the inclusion boundaries. Considering the inner inclusion 1, bounded by a surface S_1 (see Figure 2) and subjected to an incident temperature field t_{inc}, the boundary integral equation can be constructed by applying the reciprocity theorem (e.g. Manolis and Beskos [43]), leading to

(a) *the exterior domain of inclusion 1* (*Medium 1*)

$$ct^{(1)}(x_0, y_0, \omega) = \int_{S_1} q^{(1)}(x, y, \boldsymbol{n}_{n1}, \omega) G^{(1)}(x, y, x_0, y_0, \omega)\, \mathrm{d}s - \int_{S_1} H^{(1)}(x, y, \boldsymbol{n}_{n1}, x_0, y_0, \omega) t^{(1)}(x, y, \omega)\, \mathrm{d}s + t_{\text{inc}}(x_0, y_0, x_s, y_s, \omega) \quad (4)$$

In these equations, the superscript 1 corresponds to the exterior domain (Medium 1); $\boldsymbol{n}_{n1}$ is the unit outward normal along the boundary S_1; G and H are, respectively, the fundamental solutions (Green's functions) for temperature (t) and heat flux (q), at (x, y) due to a virtual heat source at (x_0, y_0). t_{inc} represents the incident heat field at (x_0, y_0) when the heat source is located at (x_s, y_s). The factor c is a constant defined by the shape of the boundary, taking the value $\frac{1}{2}$ if $(x_0, y_0) \in S_1$ and S_1 is smooth.

Equation (4) does not yet take into account the presence of the neighboring inclusion 2, which is modeled using the MFS. The MFS assumes that the response of this neighboring inclusion is found as a linear combination of fundamental solutions simulating the temperature field generated by two sets of NS virtual sources. These virtual loads are distributed along the inclusion interface

Copyright © 2010 John Wiley & Sons, Ltd.

DOI: 10.1002/nme

at distances δ from that boundary toward the interior and the exterior of the inclusion (lines $\hat{C}^{(1)}$ and $\hat{C}^{(2)}$ in Figure 2) in order to avoid singularities. Sources inside and outside the inclusion have unknown amplitudes $a^{(2)}_{n\_\text{ext}}$ and $a^{(2)}_{n\_\text{int}}$, respectively. In the exterior and interior fluid media, the temperature fields are given by

$$\begin{aligned} t^{(1)}(x,y,\omega) &= \sum_{n\_\text{ext}=1}^{\text{NS}} [a^{(2)}_{n\_\text{ext}} G^{(1)}(x,y,x_{n\_\text{ext}},y_{n\_\text{ext}},\omega)] \\ t^{(3)}(x,y,\omega) &= \sum_{n\_\text{int}=1}^{\text{NS}} [a^{(2)}_{n\_\text{int}} G^{(3)}(x,y,x_{n\_\text{int}},y_{n\_\text{int}},\omega)] \end{aligned} \tag{5}$$

where $G^{(1)}(x,y,x_{n\_\text{ext}},y_{n\_\text{ext}},\omega)$ and $G^{(3)}(x,y,x_{n\_\text{int}},y_{n\_\text{int}},\omega)$ are the fundamental solutions, which represent the temperatures at points (x,y) in Media 1 and 3, generated by heat sources acting at positions $(x_{n\_\text{ext}},y_{n\_\text{ext}})$ and $(x_{n\_\text{int}},y_{n\_\text{int}})$. n_ext and n_int are the subscripts that denote the load order number placed along lines $\hat{C}^{(1)}$ and $\hat{C}^{(2)}$, respectively.

The heat field generated by this second inclusion can be viewed as an incident field that strikes the first inclusion. Hence Equation (4) needs to be modified accordingly,

$$\begin{aligned} ct^{(1)}(x_0,y_0,\omega) = &\int_{S_1} q^{(1)}(x,y,\boldsymbol{n}_{n1},\omega) G^{(1)}(x,y,x_0,y_0,\omega)\,\mathrm{d}s \\ &- \int_{S_1} H^{(1)}(x,y,\boldsymbol{n}_{n1},x_0,y_0,\omega)\, t^{(1)}(x,y,\omega)\,\mathrm{d}s + t_{\text{inc}}(x_0,y_0,x_s,y_s,\omega) \\ &+ \sum_{n\_\text{ext}=1}^{\text{NS}} [a^{(2)}_{n\_\text{ext}} G^{(1)}(x,y,x_{n\_\text{ext}},y_{n\_\text{ext}},\omega)] \end{aligned} \tag{6}$$

(b) *the interior domain of inclusion 1* (*Medium 2*)

$$\begin{aligned} c\,t^{(2)}(x_0,y_0,\omega) = &\int_{S_1} q^{(2)}(x,y,-\boldsymbol{n}_{n1},\omega) G^{(2)}(x,y,x_0,y_0,\omega)\,\mathrm{d}s \\ &- \int_{S_1} H^{(2)}(x,y,-\boldsymbol{n}_{n1},x_0,y_0,\omega)\, t^{(2)}(x,y,\omega)\,\mathrm{d}s \end{aligned} \tag{7}$$

In Equations (7), the superscript 2 corresponds to the domain inside inclusion 1.

(c) *the interior and exterior domain of inclusion 2* (*Media 1 and 3*)

To determine the amplitudes of the unknown virtual temperature sources, $a^{(2)}_{n\_\text{ext}}$ and $a^{(2)}_{n\_\text{int}}$, the continuity of temperature and heat flux has to be imposed at interface S_2, the boundary of inclusion 2 and at NS collocation points $(x_{\text{col}},y_{\text{col}})$. This can be achieved by taking into account the heat field generated at inclusion 1. The following two equations are then defined:

$$\int_{S_1} q^{(1)}(x,y,\boldsymbol{n}_{n1},\omega) G^{(1)}(x,y,x_{\text{col}},y_{\text{col}},\omega)\,\mathrm{d}s - \int_{S_1} H^{(1)}(x,y,\boldsymbol{n}_{n1},x_{\text{col}},y_{\text{col}},\omega) t^{(1)}(x,y,\omega)\,\mathrm{d}s$$

$$+ t_{\text{inc}}(x_{\text{col}},y_{\text{col}},x_s,y_s,\omega) + \sum_{n\_\text{ext}=1}^{\text{NS}} [a^{(2)}_{n\_\text{ext}} G^{(1)}(x_{\text{col}},y_{\text{col}},x_{n\_\text{ext}},y_{n\_\text{ext}},\omega)]$$

Copyright © 2010 John Wiley & Sons, Ltd.

DOI: 10.1002/nme

$$= \sum_{n\_\text{int}=1}^{\text{NS}} [a^{(2)}_{n\_\text{int}} G^{(3)}(x_{\text{col}}, y_{\text{col}}, x_{n\_\text{int}}, y_{n\_\text{int}}, \omega)] \tag{8}$$

$$\int_{S_1} q^{(1)}(x, y, \boldsymbol{n}_{n1}, \omega) \frac{\partial G^{(1)}}{\partial \boldsymbol{n}_{n2}}(x, y, \boldsymbol{n}_{n2}, x_{\text{col}}, y_{\text{col}}, \omega)\, \mathrm{d}s$$

$$- \int_{S_1} \frac{\partial H^{(1)}}{\partial \boldsymbol{n}_{n2}}(x, y, \boldsymbol{n}_{n1}, \boldsymbol{n}_{n2}, x_{\text{col}}, y_{\text{col}}, \omega) t^{(1)}(x, y, \omega)\, \mathrm{d}s + \frac{\partial t_{\text{incl}}}{\partial \boldsymbol{n}_{n2}}(x_{\text{col}}, y_{\text{col}}, \boldsymbol{n}_{n2}, x_s, y_s, \omega)$$

$$+ \sum_{n\_\text{ext}=1}^{\text{NS}} \left[a^{(2)}_{n\_\text{ext}} \frac{\partial G^{(1)}}{\partial \boldsymbol{n}_{n2}}(x_{\text{col}}, y_{\text{col}}, \boldsymbol{n}_{n2}, x_{n\_\text{ext}}, y_{n\_\text{ext}}, \omega) \right]$$

$$= \sum_{n\_\text{int}=1}^{\text{NS}} \left[a^{(2)}_{n\_\text{int}} \frac{k_3}{k_1} \frac{\partial G^{(3)}}{\partial \boldsymbol{n}_{n2}}(x_{\text{col}}, y_{\text{col}}, \boldsymbol{n}_{n2}, x_{n\_\text{int}}, y_{n\_\text{int}}, \omega) \right] \tag{9}$$

In these equations, $\boldsymbol{n}_{n2}$ is the unit outward normal along the boundary S_2.

(d) *final system of equations*

The global solution is obtained by solving Equations ((6)–(9)). This requires the discretization of the interface S_1, the boundary of inclusion 1. In this analysis, the interface is discretized with N straight boundary elements, with one nodal point in the middle of each.

The required 2D Green's functions for temperature and temperature gradients in Cartesian co-ordinates are those for an unbounded solid medium, and they are,

$$G^{(m)}(x, y, x_k, y_k, \omega) = \frac{-\mathrm{i}}{4} H_0(k_{\alpha_m} r)$$

$$H^{(m)}(x, y, \boldsymbol{n}_{n1}, x_k, y_k, \omega) = \frac{\mathrm{i}}{4} k_{\alpha_m} H_1(k_{\alpha_m} r) \frac{\partial r}{\partial \boldsymbol{n}_{n1}}$$

$$\frac{\partial G^{(m)}}{\partial \boldsymbol{n}_{n2}}(x, y, \boldsymbol{n}_{n2}, x_k, y_k, \omega) = \frac{\mathrm{i}}{4} k_{\alpha_m} H_1(k_{\alpha_m} r) \frac{\partial r}{\partial \boldsymbol{n}_{n2}}$$

$$\frac{\partial H^{(m)}}{\partial \boldsymbol{n}_{n2}}(x, y, \boldsymbol{n}_{n1}, \boldsymbol{n}_{n2}, x_k, y_k, \omega) = \frac{\mathrm{i}}{4} k_{\alpha_m} \left\{ \begin{array}{l} \left[\dfrac{1}{r} H_1(k_{\alpha_m} r) - k_{\alpha_m} H_2(k_{\alpha_m} r) \right] \\ \quad \times \dfrac{\partial r}{\partial \boldsymbol{n}_{n1}} \dfrac{\partial r}{\partial \boldsymbol{n}_{n2}} + \dfrac{H_1(k_{\alpha_m} r)}{r} \\ \quad \times \left[\begin{array}{l} \left(\dfrac{\partial r}{\partial y} \right)^2 \dfrac{\partial x}{\partial \boldsymbol{n}_{n1}} \dfrac{\partial x}{\partial \boldsymbol{n}_{n2}} \\ - \dfrac{\partial r}{\partial y} \dfrac{\partial r}{\partial x} \left(\dfrac{\partial x}{\partial \boldsymbol{n}_{n1}} \dfrac{\partial y}{\partial \boldsymbol{n}_{n2}} + \dfrac{\partial x}{\partial \boldsymbol{n}_{n2}} \dfrac{\partial y}{\partial \boldsymbol{n}_{n1}} \right) \\ + \left(\dfrac{\partial r}{\partial x} \right)^2 \dfrac{\partial y}{\partial \boldsymbol{n}_{n1}} \dfrac{\partial y}{\partial \boldsymbol{n}_{n2}} \end{array} \right] \end{array} \right\} \tag{10}$$

Copyright © 2010 John Wiley & Sons, Ltd.

DOI: 10.1002/nme

in which $r=\sqrt{(x-x_k)^2+(y-y_k)^2}$ (where (x_k, y_k) identifies the loaded point). The thermal diffusivities in these equations are the ones associated with the exterior and the interior fluids of the inclusions ($m=1,\ 2$).

The required integrations in Equations (6)–(9) are evaluated using a Gaussian quadrature scheme when they are not performed along the loaded element. For the loaded element, the existing singular integrands in the source terms of Green's functions are calculated analytically, following the expressions in Tadeu *et al.* [44],

$$\int_0^{L/2} H_0(k_\alpha r)\,\mathrm{d}r = \frac{L}{2}H_0\left(k_\alpha\frac{L}{2}\right)+\pi\frac{L}{4}\left[H_1\left(k_\alpha\frac{L}{2}\right)S_0\left(k_\alpha\frac{L}{2}\right)-H_0\left(k_\alpha\frac{L}{2}\right)S_1\left(k_\alpha\frac{L}{2}\right)\right] \tag{11}$$

where $S_{\mathrm{ns}}(\ldots)$ are Struve functions of order ns and L is the boundary element length.

The final integral equations are manipulated and combined so as to impose the continuity of temperatures and heat fluxes along the boundary of inclusions 1 and 2, to establish a system of $[(2NS+2N)\times(2NS+2N)]$ equations. The solution of this system of equations gives the nodal temperatures and heat fluxes along boundary S_1 and the unknown virtual temperature source amplitudes $a^{(2)}_{n\_\mathrm{ext}}$ and $a^{(2)}_{n\_int}$, which allow the temperature field to be defined inside and outside the inclusions.

2.1.2. Null heat fluxes along their boundaries. In this case, the boundary conditions prescribe null normal temperature gradients along boundaries S_1 and S_2. Thus, Equations (6)–(9) are simplified to

$$\begin{aligned} ct^{(1)}(x_0,y_0,\omega) = &-\int_{S_1} H^{(1)}(x,y,\boldsymbol{n}_{n1},x_0,y_0,\omega)\,p^{(1)}(x,y,\omega)\,\mathrm{d}s \\ &+t_{\mathrm{inc}}(x_0,y_0,x_s,y_s,\omega)+\sum_{n\_\mathrm{ext}=1}^{\mathrm{NS}}\left[a^{(2)}_{n\_\mathrm{ext}}G^{(1)}(x,y,x_{n\_\mathrm{ext}},y_{n\_\mathrm{ext}},\omega)\right] \end{aligned} \tag{12}$$

$$\begin{aligned} &-\int_{S_1}\frac{\partial H^{(1)}}{\partial \boldsymbol{n}_{n2}}(x,y,\boldsymbol{n}_{n1},\boldsymbol{n}_{n2},x_{\mathrm{col}},y_{\mathrm{col}},\omega)\,t^{(1)}(x,y,\omega)\,\mathrm{d}s+\frac{\partial t_{\mathrm{inc}}}{\partial \boldsymbol{n}_{n2}}(x_{\mathrm{col}},y_{\mathrm{col}},\boldsymbol{n}_{n2},x_s,y_s,\omega) \\ &+\sum_{n\_\mathrm{ext}=1}^{\mathrm{NS}}\left[a^{(2)}_{n\_\mathrm{ext}}\frac{\partial G^{(1)}}{\partial \boldsymbol{n}_{n2}}(x_{\mathrm{col}},y_{\mathrm{col}},\boldsymbol{n}_{n2},x_{n\_\mathrm{ext}},y_{n\_\mathrm{ext}},\omega)\right]=0 \end{aligned} \tag{13}$$

The solution of this integral for the boundary surfaces (S_1) again requires the discretization of the boundary inclusion 1 into N straight boundary elements and the simulation of inclusion 2 using NS collocation points/virtual heat sources, following a procedure similar to the one described above. This gives a system of $[(NS+N)\times(NS+N)]$ equations.

2.1.3. Null temperatures along their boundaries. Null temperatures are now prescribed at the surface of the inclusions, which leads to the following equations:

$$\begin{aligned} &\int_{S_1} q^{(1)}(x,y,\boldsymbol{n}_{n1},\omega)G^{(1)}(x,y,x_0,y_0,\omega)\,\mathrm{d}s \\ &+t_{\mathrm{inc}}(x_0,y_0,x_s,y_s,\omega)+\sum_{n\_\mathrm{ext}=1}^{\mathrm{NS}}\left[a^{(2)}_{n\_\mathrm{ext}}G^{(1)}(x,y,x_{n\_\mathrm{ext}},y_{n\_\mathrm{ext}},\omega)\right]=0 \end{aligned} \tag{14}$$

Copyright © 2010 John Wiley & Sons, Ltd.

DOI: 10.1002/nme

$$\int_{S_1} q^{(1)}(x, y, \boldsymbol{n}_{n1}, \omega) G^{(1)}(x, y, x_{\text{col}}, y_{\text{col}}, \omega)\, \mathrm{d}s$$

$$+ t_{\text{inc}}(x_{\text{col}}, y_{\text{col}}, x_s, y_s, \omega) + \sum_{n\_\text{ext}=1}^{\text{NS}} [a^{(2)}_{n\_\text{ext}} G^{(1)}(x_{\text{col}}, y_{\text{col}}, x_{n\_\text{ext}}, y_{n\_\text{ext}}, \omega)] = 0 \tag{15}$$

The solution of this equation is once again obtained as described before.

Other combinations of inclusions can be solved by simplifying Equations (6)–(9) according to the required boundary conditions.

2.2. *TBEM/MFS coupling formulation*

The TBEM can be formulated applying dipoles, or dynamic doublets, to the heat boundary integral equations [32], leading to the following equations (16)–(17) that replace Equations (6)–(7) when modeling the first inclusion:

$$\begin{aligned} & a t^{(1)}(x_0, y_0, \omega) + c\, q^{(1)}(x_0, y_0, \boldsymbol{n}_{n1}, \omega) \\ & = \int_{S_1} q^{(1)}(x, y, \boldsymbol{n}_{n1}, \omega) \overline{G}^{(1)}(x, y, \boldsymbol{n}_{n2}, x_0, y_0, \omega)\, \mathrm{d}s \\ & \quad - \int_{S_1} \overline{H}^{(1)}(x, y, \boldsymbol{n}_{n1}, \boldsymbol{n}_{n2}, x_0, y_0, \omega) t^{(1)}(x, y, \omega)\, \mathrm{d}s + \bar{t}_{\text{inc}}(x_0, y_0, \boldsymbol{n}_{n2}, x_s, y_s, \omega) \\ & \quad + \sum_{n\_\text{ext}=1}^{\text{NS}} [a^{(2)}_{n\_\text{ext}} \bar{G}^{(1)}(x, y, \boldsymbol{n}_{n2}, x_{n\_\text{ext}}, y_{n\_\text{ext}}, \omega)] \end{aligned} \tag{16}$$

$$\begin{aligned} & a t^{(2)}(x_0, y_0, \omega) + c\, q^{(2)}(x_0, y_0, \boldsymbol{n}_{n1}, \omega) \\ & = \int_{S_1} q^{(2)}(x, y, \boldsymbol{n}_{n1}, \omega) \overline{G}^{(2)}(x, y, \boldsymbol{n}_{n2}, x_0, y_0, \omega)\, \mathrm{d}s \\ & \quad - \int_{S_1} \overline{H}^{(2)}(x, y, \boldsymbol{n}_{n1}, \boldsymbol{n}_{n2}, x_0, y_0, \omega) t^{(2)}(x, y, \omega)\, \mathrm{d}s \end{aligned} \tag{17}$$

Equations (8)–(9) can be kept the same. As noted by Guiggiani [45], the coefficient a is zero for piecewise straight boundary elements. Factor c is a constant defined as above.

The solutions of these equations are defined as before by discretizing the S_1 surface into N straight boundary elements, with one nodal point in the middle of each element. The required 2D Green's functions are now

$$\overline{G}^{(m)}(x, y, \boldsymbol{n}_k, x_k, y_k, \omega) = \frac{\mathrm{i}}{4} k_{\alpha_m} H_1(k_{\alpha_m} r) \frac{\partial r}{\partial n_k}$$

Copyright © 2010 John Wiley & Sons, Ltd.

DOI: 10.1002/nme

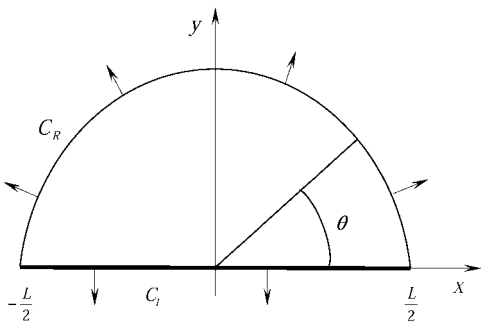

Figure 3. Energy equilibrium on the boundary element being loaded.

$$\begin{aligned}
&\bar{H}^{(m)}(x, y, \boldsymbol{n}_l, \boldsymbol{n}_k, x_k, y_k, \omega) \\
&= \frac{\mathrm{i}}{4} k_{\alpha m} \left\{ -k_{\alpha m} H_2(k_{\alpha m} r) \left[\left(\frac{\partial r}{\partial x} \right)^2 \frac{\partial x}{\partial \boldsymbol{n}_l} + \frac{\partial r}{\partial x} \frac{\partial r}{\partial y} \frac{\partial y}{\partial \boldsymbol{n}_l} \right] + \frac{H_1(k_{\alpha m} r)}{r} \left[\frac{\partial x}{\partial \boldsymbol{n}_l} \right] \right\} \frac{\partial x}{\partial \boldsymbol{n}_k} \\
&\quad + \frac{\mathrm{i}}{4} k_{\alpha m} \left\{ -k_{\alpha m} H_2(k_{\alpha m} r) \left[\frac{\partial r}{\partial x} \frac{\partial r}{\partial y} \frac{\partial x}{\partial \boldsymbol{n}_l} + \left(\frac{\partial r}{\partial y} \right)^2 \frac{\partial y}{\partial \boldsymbol{n}_l} \right] + \frac{H_1(k_{\alpha m} r)}{r} \left[\frac{\partial y}{\partial \boldsymbol{n}_l} \right] \right\} \frac{\partial y}{\partial \boldsymbol{n}_k}
\end{aligned} \tag{18}$$

where $\boldsymbol{n}_k$ and $\boldsymbol{n}_l$ are the unit outward normal for the boundary segments being loaded and integrated, respectively. In Equation (16), the incident field is computed by

$$\bar{t}_{\mathrm{inc}}(x, y, \boldsymbol{n}_k, x_s, y_s, \omega) = \frac{\mathrm{i}A}{2} k_\alpha H_1(k_\alpha r_1) \left(\frac{x - x_s}{r_1} \frac{\partial x}{\partial \boldsymbol{n}_k} + \frac{y - y_s}{r_1} \frac{\partial y}{\partial \boldsymbol{n}_k} \right). \tag{19}$$

The integrations in Equations (16) and (17) are performed through a Gaussian quadrature scheme when the element being integrated is not the loaded one. When the element being integrated (C_l) is the loaded one, the following integral becomes hypersingular:

$$\begin{aligned}
&\int_{C_l} \bar{H}^{(m)}(x, y, \boldsymbol{n}_l, \boldsymbol{n}_l, x_k, y_k, \omega)\, \mathrm{d}C_l \\
&= \int_{C_l} \frac{\mathrm{i}}{4} k_{\alpha m} \left[-k_\alpha H_2(k_{\alpha m} r) \left(\frac{\partial r}{\partial x} \frac{\partial x}{\partial \boldsymbol{n}_l} + \frac{\partial r}{\partial y} \frac{\partial y}{\partial \boldsymbol{n}_l} \right)^2 + \frac{H_1(k_{\alpha m} r)}{r} \right] \mathrm{d}C_l
\end{aligned} \tag{20}$$

This integral can be evaluated analytically, considering the dynamic energy equilibrium of a semi-cylinder bounded by the boundary element, as illustrated in Figure 3.

The equilibrium is established by assuming that the change in the internal energy within the material inside the semi-cylinder equals the heat leaving the domain and crossing the boundary element and the surface of the semi-cylinder.

$$\begin{aligned}
&\int_{C_l} \bar{H}^{(m)}(x, y, \boldsymbol{n}_l, \boldsymbol{n}_l, x_k, y_k, \omega)\, \mathrm{d}C_l \\
&= \int_{C_R} \frac{L}{2} \frac{\partial \overline{G}^{(m)}(x, y, \boldsymbol{n}_k, x_k, y_k, \omega)}{\partial r} \bigg|_{L/2} \mathrm{d}C_R - \int_A \frac{\rho_m c_m}{k_m} \frac{\partial \overline{G}^{(m)}(x, y, \boldsymbol{n}_k, x_k, y_k, \omega)}{\partial t} \mathrm{d}A
\end{aligned} \tag{21}$$

Copyright © 2010 John Wiley & Sons, Ltd.

DOI: 10.1002/nme

where A is the domain between the boundary element (C_l) and the semi-cylinder surface (C_R).

Both integrands on the right side of Equation (21) are well behaved and can be evaluated directly.

$$\int_{C_R} \frac{L}{2} \frac{\partial \overline{G}^{(m)}(x, y, \boldsymbol{n}_k, x_k, y_k, \omega)}{\partial r}\bigg|_{L/2} \mathrm{d}C_R = \frac{\mathrm{i}}{2} k_{\alpha m}^2 \left[\frac{L}{2} H_0\left(k_{\alpha m} \frac{L}{2}\right) - \frac{1}{k_{\alpha m}} H_1\left(k_{\alpha m} \frac{L}{2}\right)\right] \tag{22}$$

$$\int_A \frac{\rho_m c_m}{k_m} \frac{\partial \overline{G}^{(m)}(x, y, \boldsymbol{n}_k, x_k, y_k, \omega)}{\partial t} \mathrm{d}A = \int_0^{L/2} \int_0^{\pi} \frac{\rho_m c_m}{k_m} (\mathrm{i}\omega) \frac{\mathrm{i}}{4} k_{\alpha m} H_1(k_{\alpha m} r) \sin(\theta) r \, \mathrm{d}r \, \mathrm{d}\theta$$

$$= \frac{\mathrm{i}}{2} k_{\alpha m}^2 \left[\int_0^{L/2} H_0(k_{\alpha m} r) \, \mathrm{d}r - \frac{1}{k_{\alpha m}} H_1\left(k_{\alpha m} \frac{L}{2}\right)\right] \tag{23}$$

This leads to

$$\int_{C_l} \bar{H}^{(m)}(x, y, \boldsymbol{n}_l, \boldsymbol{n}_k, x_k, y_k, \omega) \, \mathrm{d}C_l = \frac{\mathrm{i}}{2} (k_{\alpha m})^2 \left[\int_0^{L/2} H_0(k_{\alpha m} r) \, \mathrm{d}r - \frac{1}{k_{\alpha m}} H_1\left(k_{\alpha m} \frac{L}{2}\right)\right] \tag{24}$$

where L stands for the length of the boundary element. The integral $\int_0^{L/2} H_0(k_{\alpha m} r) \, \mathrm{d}r$ is evaluated as indicated above. The final system of equations is obtained by combining Equations (8)–(9), and (16)–(17) and imposing the continuity of temperatures and heat fluxes along the boundary of inclusions 1 and 2.

Manipulating Equations (8)–(9) and (16)–(17) as described above, null temperature and null heat fluxes can be ascribed along the inclusions' boundaries.

The present TBEM formulation overcomes the thin-body difficulty for which the classical direct BEM formulation degenerates. The direct application of this method allows empty or thin inclusions to be modeled using a single line representation. Where null heat fluxes or null temperatures are ascribed to null-thickness inclusions, the results identify the temperatures or heat gradient jumps between the two sides of the element.

2.3. (Combined BEM+TBEM)/ MFS coupling formulation

The TBEM and the BEM formulations can be combined so as to solve the problems described above. But this technique allows the solution to be defined when inclusion 1 is a thin solid-filled inclusion. A part of the boundary surface of that inclusion is loaded with monopole loads, whereas the rest is loaded with dipoles. In this case, the thin bodies can be solved using a closed surface.

3. VERIFICATION AND COMPUTATIONAL EFFICIENCY OF THE COUPLING ALGORITHMS

This section illustrates first the corroboration of the proposed coupling algorithms [BEM/MFS, TBEM/MFS and (combined BEM+TBEM)/MFS] using systems composed of circular cylindrical inclusions, for which analytical solutions are known. Then the coupling algorithms solutions are verified by solving the problem of a ring system incorporating a thin defect, a crack, for which

Copyright © 2010 John Wiley & Sons, Ltd.

DOI: 10.1002/nme

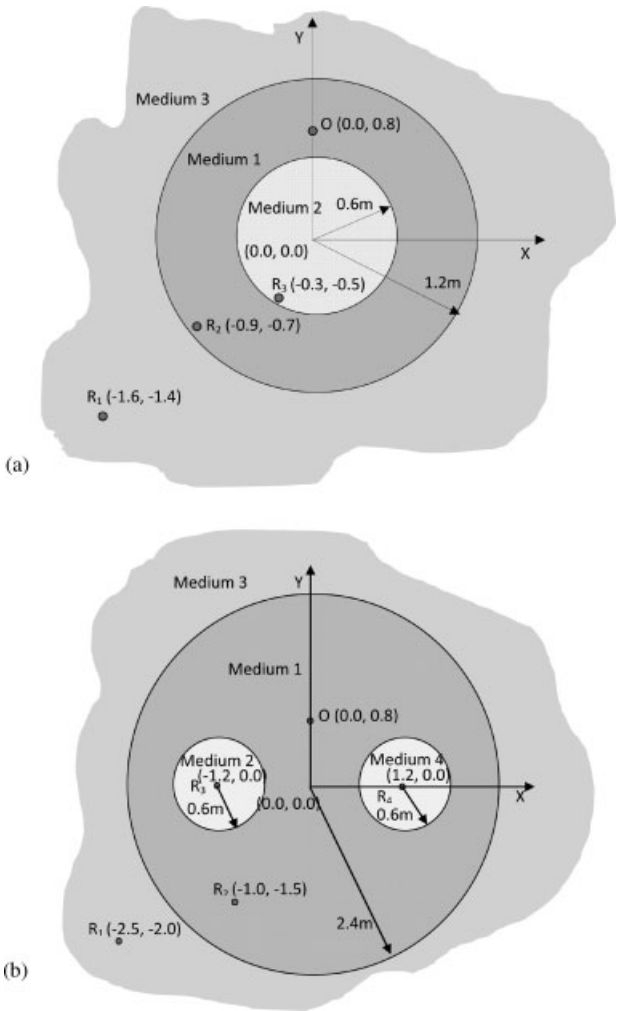

Figure 4. Systems used to verify the proposed coupling solutions: (a) circular cylindrical system composed of three concentric circular sections and (b) system composed by a cylindrical inclusion embedded in a spatially uniform unbounded medium that hosts two smaller inclusions.

analytical solutions are not known. This example is also used to assess the computational efficiency benefits of using the proposed coupling algorithms.

3.1. Systems composed of circular cylindrical inclusions

First, a circular cylindrical ring core, composed of three layers of different materials (Media 1–3), as illustrated in Figure 4(a), is excited by a harmonic line heat source. The solution for this problem is known in closed form. It is obtained by applying a technique equivalent to the separation of variables procedure to the Helmholtz equation given by Equation (2) to each medium in the system.

Copyright © 2010 John Wiley & Sons, Ltd.

DOI: 10.1002/nme

Table I. Thermal material properties.

	Thermal conductivity, k ($W \cdot m^{-1} \cdot {}^{\circ}C^{-1}$)	Density, ρ ($kg \cdot m^{-3}$)	Specific heat, c ($J \cdot kg^{-1} \cdot {}^{\circ}C^{-1}$)
Medium 1 (concrete)	1.40	2300.0	880.0
Medium 2 (steel)	52.9	7860.0	486.0
Medium 3 (air)	0.026	1.2928	1000.0
Medium 4 (polystyrene)	0.035	35.0	1400.0
Medium 5	1.0	1.0	1.0×10^{-4}
Medium 6	10.0	1.0	1.0×10^{-4}
Medium 7	10.0	1.0	1.0×10^{-2}

The boundary conditions are enforced along all interfaces by using the form of a series of Bessel functions (see Appendix A).

The proposed coupling solutions are then verified by computing the heat diffusion in a system composed of a circular solid inclusion (Medium 1), buried in an unbounded fluid Medium (Medium 3) hosting two other circular inclusions made of different materials (Media 2 and 4) (see Figure 4(b)). The responses are compared against analytical solutions obtained by applying, as above, the separation of variables method to the Helmholtz equation in each medium, following the technique described by Gordeliy *et al.* [46]. Appendix B outlines the way in which the solution is computed.

The thermal properties of the different media remain constant in all simulations and are listed in Table I.

All the calculations are performed in the frequency range $[0.0, 1.5 \times 10^{-8}]$ Hz with a frequency increment of $\Delta\omega = 1 \times 10^{-10}$ Hz, and the imaginary part of the frequency is given by $\eta = 0.7\Delta\omega$.

3.1.1. Circular cylindrical system with three concentric circular sections. The circular interface of the inner media that separates Medium 1 from Medium 2 (the core Medium) has a radius of 0.6 m. The outer interface has a radius of 1.2 m and separates Medium 1 from the outer unbounded Medium 3. The harmonic line heat is placed in Medium 1 at (0.0 m, 0.8 m). Different boundary conditions are prescribed along the inner interface: continuity of temperatures and heat fluxes (Case 1) and null heat fluxes (Case 2). In both cases, continuity of temperatures and heat fluxes are imposed on the outer interface.

The temperature responses are computed at three receivers R_1–R_3 placed as illustrated in Figure 4(a). All simulations with BEM/TBEM formulation used 80 and 160 boundary elements to model the inner and the outer media interfaces, respectively, for the BEM/TBEM formulations. For the MFS, 80 and 160 virtual sources are adopted to model the inner and outer interfaces, respectively, placed at distances $0.97 \times$ radius and $1.03 \times$ radius from the center of the inclusions. Equal numbers of collocation points are evenly placed along the media interfaces. Figure 5 illustrates the position of the boundary elements, the virtual sources and the collocation points when the inner and outer interfaces are modeled with the BEM and MFS techniques.

Figures 6(a) and (b) present the real and the imaginary parts of the temperature responses for Cases 1 and 2, respectively. The lines correspond to the analytical responses (see appendix A), used here as reference solutions, whereas the different MFS and coupling solutions are represented by

Copyright © 2010 John Wiley & Sons, Ltd.

DOI: 10.1002/nme

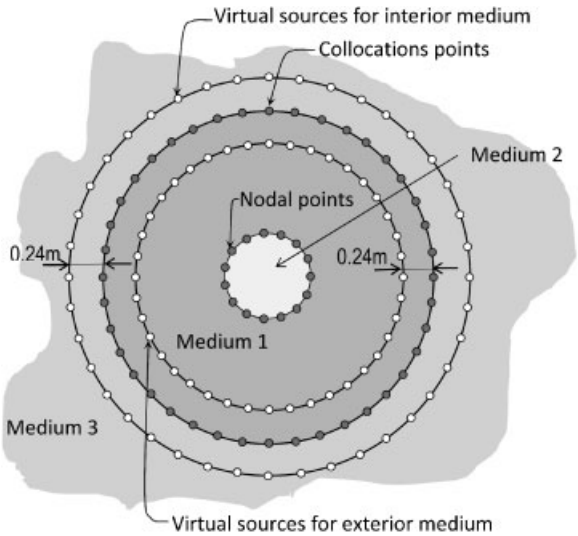

Figure 5. Position of nodal points, virtual sources and collocation points when the inner and the outer interfaces are modeled with BEM or TBEM and MFS techniques.

the marked points and labeled 'MFS/MFS', 'BEM/MFS', 'TBEM/MFS' and 'TBEM/BEM'. The solid and the dashed lines indicate, respectively, the real and the imaginary parts of the response.

Analysis of the results reveals a very good agreement between the proposed coupling solutions and the analytical, BEM and MFS models' solutions.

3.1.2. A circular cylindrical system buried in a homogeneous unbounded fluid medium, hosting two inclusions inside. As described above, in this system the circular solid inclusion with a radius of 2.4 m hosts two circular inclusions with radii of 0.6 m (see Figure 4(b)). The center of inclusion 1 is at (0.0 m, 0.0 m) and the centers of inclusion 2 (filled with polystyrene) and 3 (filled with steel) are at (−1.2 m, 0.0 m) and (1.2 m, 0.0 m), respectively. The proposed formulations are applied to two situations: first, imposing the continuity of temperatures and heat fluxes along all media interfaces (Case 3), and second, prescribing null heat fluxes along the boundary of inclusion 2 (Case 4). The harmonic line heat is placed in Medium 1 at (0.0 m, 0.8 m).

Temperature responses are obtained for four receivers R_1–R_4 placed as displayed in Figure 4(b). When the system is solved using the BEM/TBEM formulations, 80 constant boundary elements are used to discretize the inner inclusions, whereas 160 are placed along the outer interface. When the inclusions are simulated using the MFS, 80 virtual heat sources are used to model the inner inclusions and 160 are adopted to model the outer media interface, placed at distances $0.8 \times$ radius and $1.2 \times$ radius from their centers. An equal number of collocation points is used to verify the boundary conditions along the boundary interfaces.

Figures 7 and 8 present the real and imaginary parts of the temperature responses for Cases 3 and 4, respectively. The lines correspond to the analytical responses (see Appendix B), whereas the different MFS and coupling solutions are represented by the marked points and are labeled as 'MFS/MFS/MFS', 'TBEM/BEM/BEM', 'BEM/MFS/MFS' and 'TBEM/MFS/MFS'. As

Copyright © 2010 John Wiley & Sons, Ltd.

DOI: 10.1002/nme

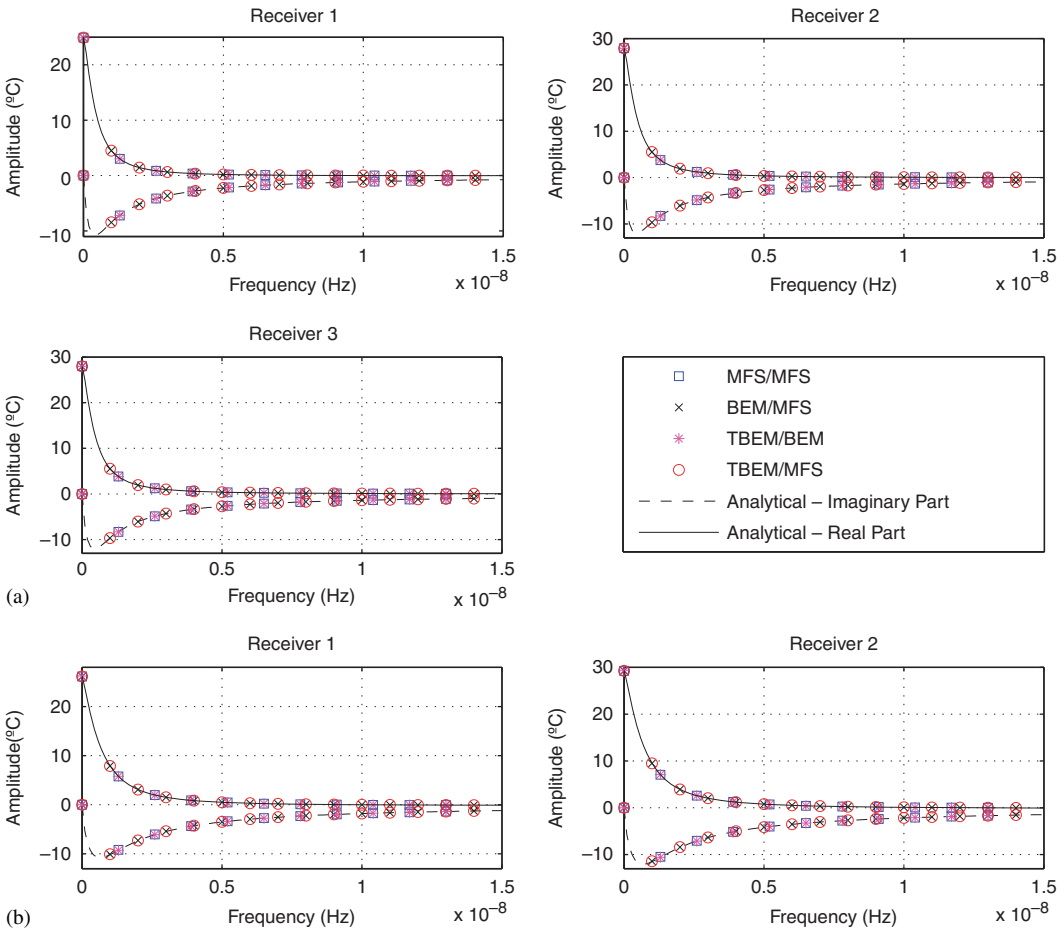

Figure 6. Analytical and BEM, MFS or TBEM coupling responses: (a) Case 1: continuity of temperatures and heat fluxes and (b) Case 2: null heat fluxes along the inner interface.

before, the solid and the dashed lines, respectively, indicate the real and the imaginary parts of the response.

Analysis of the results again reveals a very good agreement between the proposed coupling solutions and the analytical solutions. Equally good results were found when the heat sources and receivers were located in different positions.

3.2. System composed of a circular ring incorporating a thin defect

A ring system filled with solid material incorporates a thin defect, a crack, with null thickness, in its wall. The inner diameter of the ring is 0.3 m and the wall thickness is 0.2 m. The crack is placed in the middle of the ring's wall, forming a circular concentric arc of 45.0° with a radius of 0.4 m. The harmonic line heat source is placed at (0.0 m, 0.0 m) (see Figure 9(a)).

Copyright © 2010 John Wiley & Sons, Ltd.

DOI: 10.1002/nme

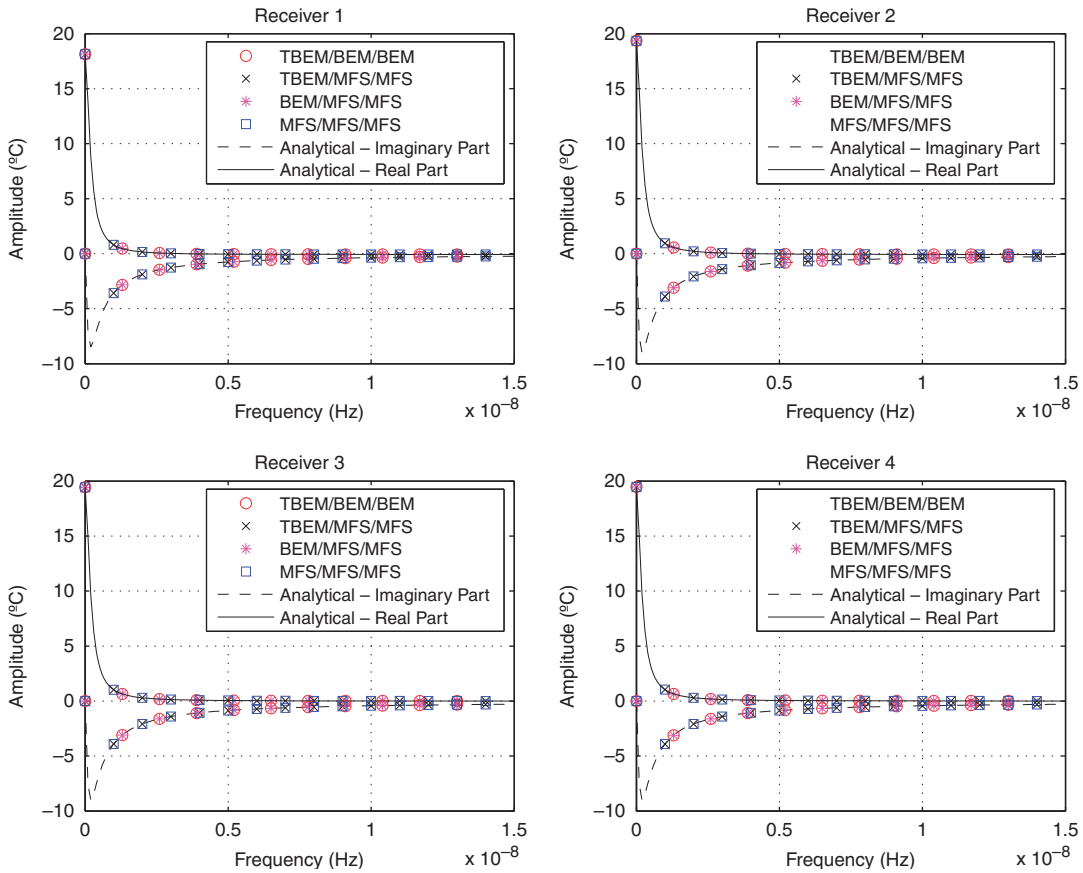

Figure 7. BEM, MFS and coupling responses—Case 3: continuity of temperatures and heat fluxes along all media interfaces.

The material thermal properties of its wall (concrete), of the solid filling the ring (steel) and of the hosting fluid medium (air) are listed in Table I.

This system is subjected to heat diffusion generated by a heat source placed in the inner medium with excitation frequencies of 0.0 Hz and 10.0^{-6} Hz, respectively. Null heat fluxes are imposed along the boundary of the defect. As there are no known analytical solutions, the BEM/TBEM solution for a large amount of boundary elements (1440 boundary elements) is used as reference solution. In this model, the null-thickness crack is discretized as an open line and loaded with dipole loads (TBEM), whereas the outer and inner interfaces are discretized using classical closed surfaces and are loaded with monopole loads (BEM). Figures 10(a) and (b) illustrate the real and the imaginary parts of the reference solutions for excitation frequencies of 0.0 Hz and 10.0^{-6} Hz, respectively. The responses have been obtained by introducing an imaginary part to the frequency given by $\eta = 0.7 \times 10.0^{-7}$.

The TBEM/MFS coupling model discretizes the crack with boundary elements loaded with dipole loads (TBEM). The inner and the outer surfaces of the ring are modeled using a set of

Copyright © 2010 John Wiley & Sons, Ltd.

DOI: 10.1002/nme

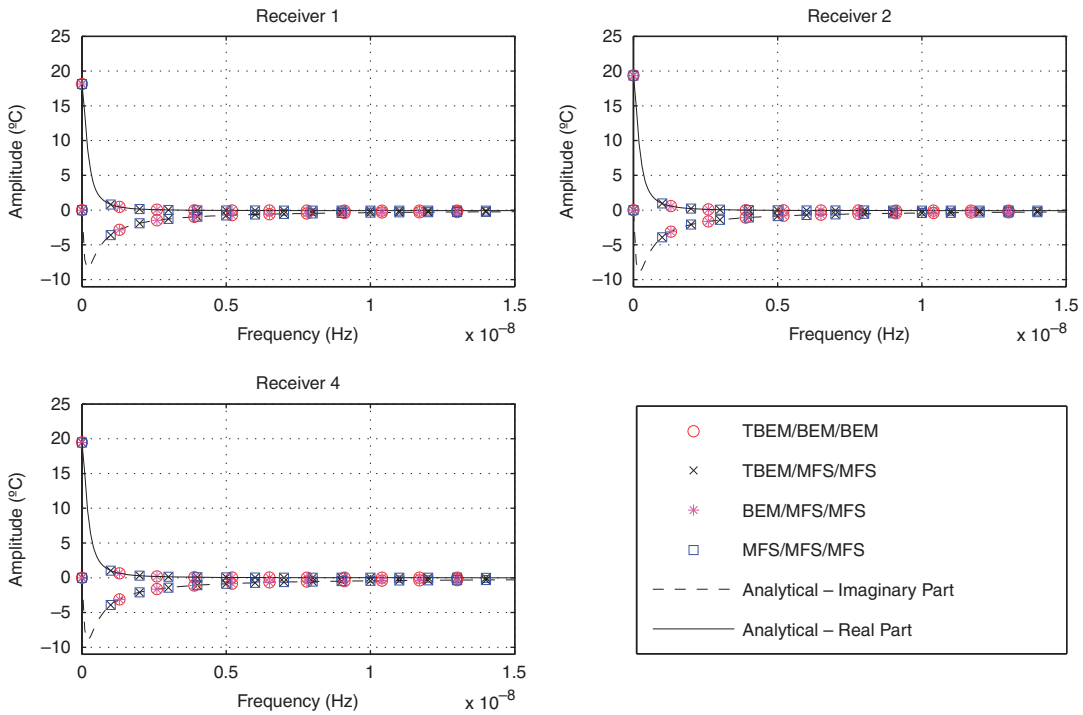

Figure 8. BEM, MFS and coupling responses—Case 4: null heat fluxes along the boundary of inclusion 2.

virtual heat sources placed at 0.05 m from the outer boundary and 0.03 m from the inner boundary. The collocation points are evenly distributed along the wall surfaces.

This system is also solved using an MFS model. The MFS is less efficient at modeling thin inclusions such as cracks. The approach used here to model the heat diffusion around the crack is based on the decomposition of the inner domain into two different sub-domains, as illustrated in Figure 9(b). The interface between these two sub-domains will be circular containing the crack, T, and a fictitious interface, F. In order to correctly describe the behavior of the null-thickness crack, null heat fluxes are ascribed to both sides of it and continuity of temperature and heat fluxes are imposed along F. The inner and the outer surfaces of the ring and the virtual interface that includes the crack are simulated placing the virtual heat sources at 0.015 m from the outer boundary, 0.009 m from the inner boundary and at 0.012 m from the virtual interface that incorporates the crack.

To assess the correctness of the solutions, the responses are calculated on a grid of 3034 receivers evenly spaced along the domain defined by a radius of 0.7 m. The MFS, TBEM/MFS and TBEM/BEM errors along the domain are assessed by comparing the responses obtained with those provided by the reference solution. A global domain error is defined by computing the integration of the volume generated by the absolute value of the difference between the reference and the different model responses along the interior grid of receivers.

To evaluate the computational efficiency, the CPU time required to compute the solution on the full grid of receivers by the three computational models is registered. All solutions have been computed on a laptop computer with an Intel® Core™ Duo CPU P9600.

Copyright © 2010 John Wiley & Sons, Ltd.

DOI: 10.1002/nme

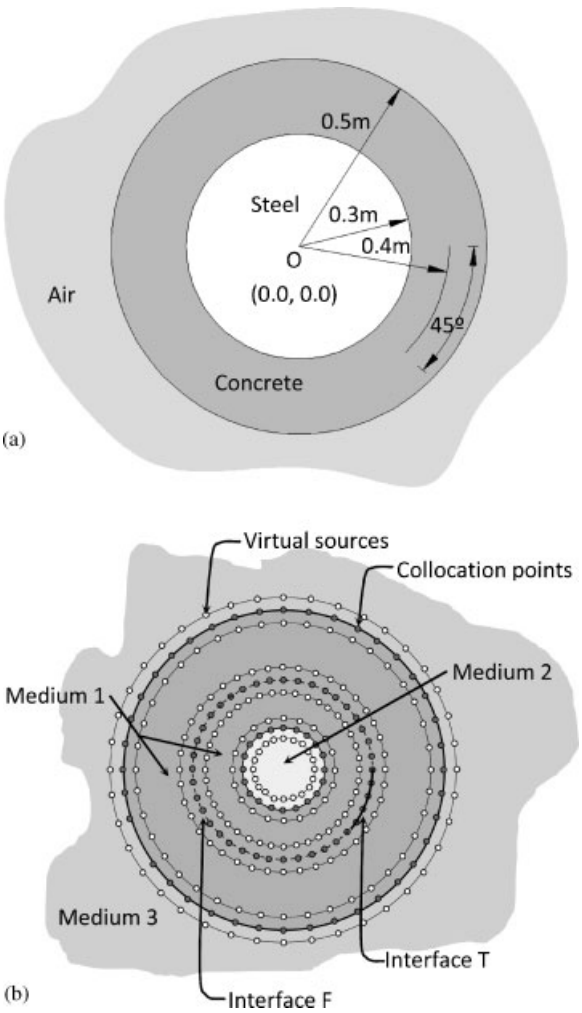

Figure 9. The ring containing a null-thickness crack: (a) geometry of the cross-section and (b) position of the nodal points, virtual sources and collocation points when all material interfaces are modeled with the MFS technique.

Figure 11 illustrates the global domain error registered versus CPU time required by each formulation, varying the number of degrees of freedom, that is, changing the number of boundary elements and virtual sources/collocation points.

For each formulation, the number of degrees of freedom varies according to the value of $n = 1$, 20, as follows: the TBEM/BEM solutions were computed discretizing the inner, the outer and the crack interfaces with $12 \times n$, $20 \times n$, and $4 \times n$ boundary elements, respectively; the TBEM/MFS solutions were obtained using $12 \times n$ and $20 \times n$ virtual sources/collocation points, to simulate the inner and the outer interfaces, respectively, and $4 \times n$ boundary elements to model the crack interface; the MFS solutions were obtained simulating the inner, the outer and the crack interfaces with $12 \times n$, $20 \times n$ and $16 \times n$ virtual sources/collocation points, respectively.

Copyright © 2010 John Wiley & Sons, Ltd.

DOI: 10.1002/nme

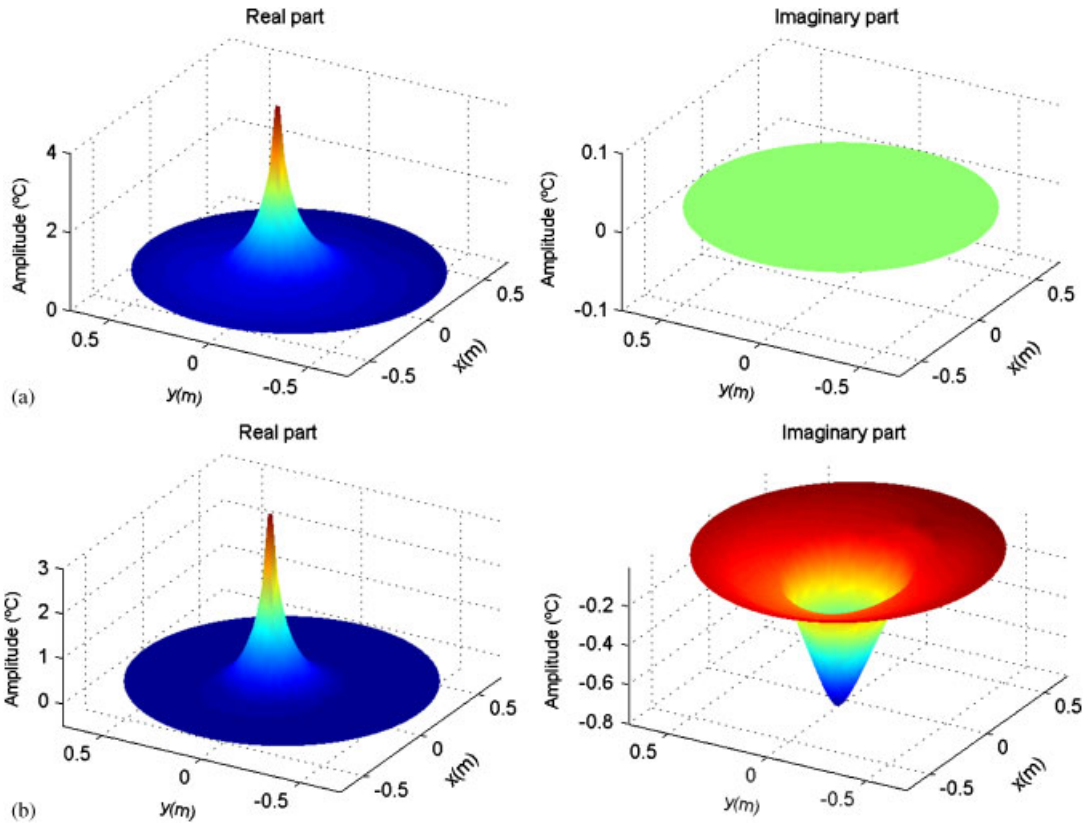

Figure 10. Reference solution for the system composed of a circular ring incorporating a thin defect. Real and imaginary parts of the response for: (a) $f = 0.0\,\text{Hz}$ and (b) $f = 10.0^{-6}\,\text{Hz}$.

The global domain errors shown in Figures 11(a) and (b) are displayed in a logarithmic scale to allow an easier interpretation of the results. An analysis of the responses shows that all responses register smaller errors with increasing number of degrees of freedom, which means, all solutions converge to the reference response. The results reveal that the coupled TBEM/MFS formulation is the algorithm that requires much less CPU time for reaching the same accuracy, except for $n = 1$ when large errors are registered. For the same number of n $(n > 1)$, the coupled TBEM/MFS solution exhibits the smallest global domain error. For the same accuracy, the computing time of the coupling algorithm is in general 5 times shorter than that taken by the TBEM/BEM formulation. On the other hand, the standard MFS formulation is the algorithm that requires most CPU time to achieve the same accuracy.

4. TEMPERATURE IN TIME-SPACE

A numerical inverse fast Fourier transform is applied in the frequency domain to find the heat field in the time domain. Aliasing phenomena are dealt by introducing complex frequencies with

Copyright © 2010 John Wiley & Sons, Ltd.

DOI: 10.1002/nme

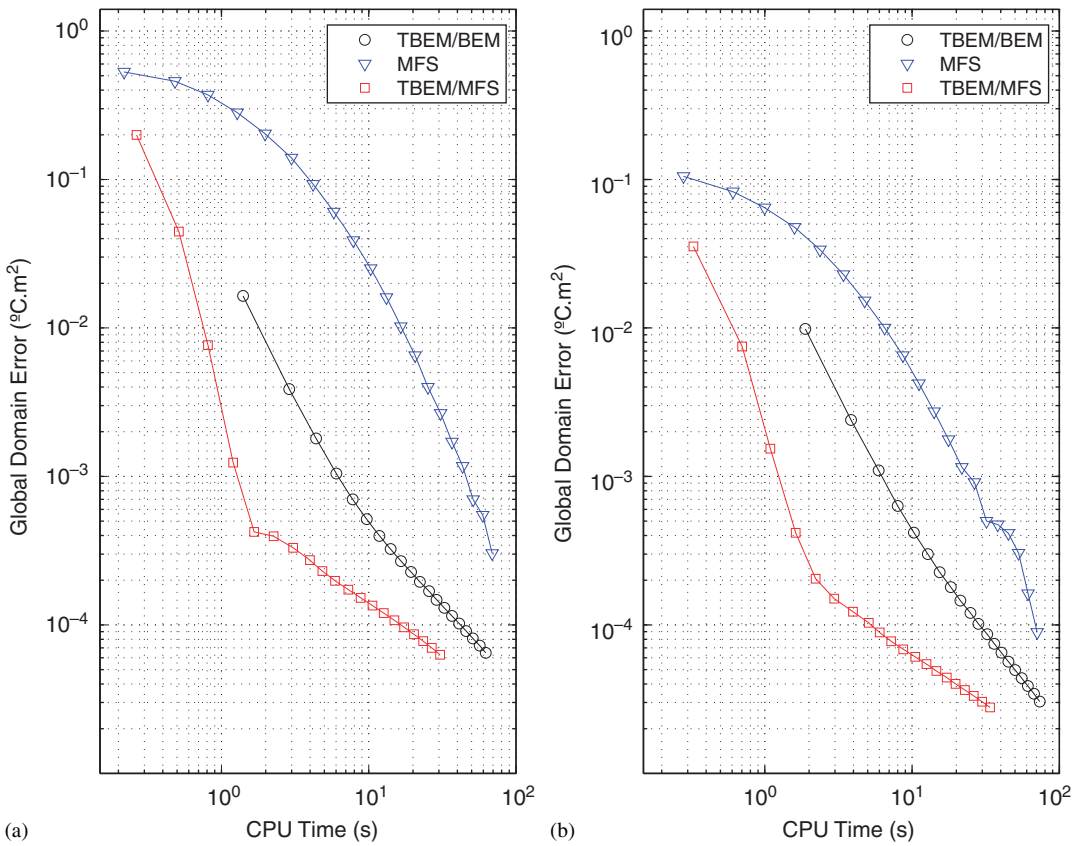

Figure 11. Global domain error versus CPU time for the system composed of a circular ring incorporating a thin defect: (a) $f=0.0\,\mathrm{Hz}$ and (b) $f=10.0^{-6}\,\mathrm{Hz}$.

a small imaginary part, taking the form $\omega_c=\omega-\mathrm{i}\eta$ (where $\eta=0.7\Delta\omega$, and $\Delta\omega$ is the frequency step). This shift is subsequently taken into account in the time domain by means of an exponential window, $\mathrm{e}^{\eta\tau}$, applied to the response.

The source can have any time variation. We can determine the frequency domain solution by applying a time Fourier transformation, and it can range from 0.0 Hz to quite high frequencies. Since the heat response falls rapidly with increasing frequency, we do not need to compute the highest frequencies in the range.

The 0.0 Hz frequency is the static response. The use of complex frequencies allows this response to be computed since the argument of the Hankel functions in the integral equations is $-\mathrm{i}\eta$, i.e. other than zero.

Discrete summations over frequencies are carried out for the Fourier transformations. Mathematically, this is the same as adding periodic sources at time intervals $T_w=2\pi/\Delta\omega$.

To verify the correctness of the solution given by this methodology, the time-dependent temperature field is compared with a reference solution. The reference solution used is the published solution provided by Gordeliy *et al.* [46] and by Furman and Neuman [47], where a line heat

Copyright © 2010 John Wiley & Sons, Ltd.

DOI: 10.1002/nme

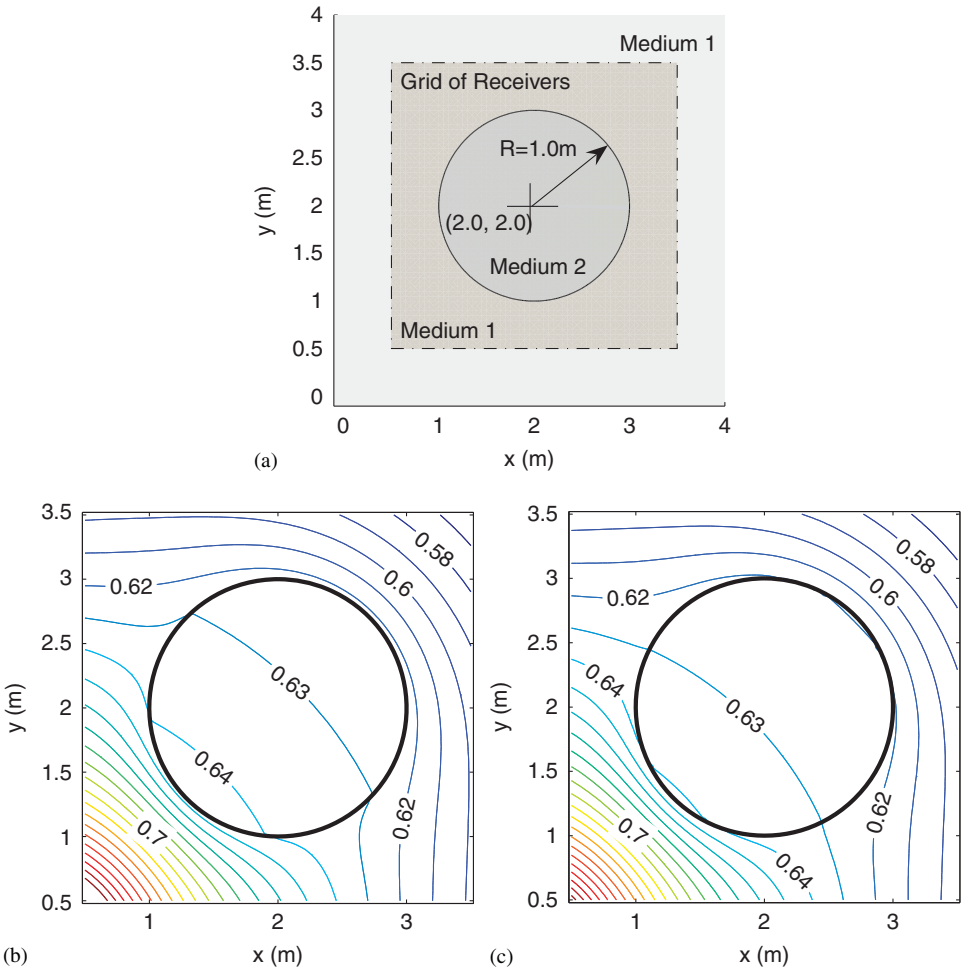

Figure 12. Verification of the time-dependent temperature field: (a) geometry of the problem: source and receivers positions; (b) temperature (in °C) contours when $c_2 = 1.0 \times 10^{-4}\,\mathrm{J \cdot kg^{-1} \cdot {}^{\circ}C^{-1}}$, $\rho_2 = 1.0\,\mathrm{kg \cdot m^{-3}}$, $k_2 = 10.0\,\mathrm{W.m^{-1} \cdot {}^{\circ}C^{-1}}$; and (c) temperature contours (in °C) when $c_2 = 1.0 \times 10^{-2}\,\mathrm{J \cdot kg^{-1} \cdot {}^{\circ}C^{-1}}$, $\rho_2 = 1.0\,\mathrm{kg \cdot m^{-3}}$, $k_2 = 10.0\,\mathrm{W \cdot m^{-1} \cdot {}^{\circ}C^{-1}}$.

source illuminates a cylindrical circular inhomogeneity placed at (2.0 m, 2.0 m) and with a radius of 1.0 m, as illustrated in Figure 12(a). The inclusion is assumed to be perfectly bonded to the unbounded medium.

The unbounded medium is characterized by a thermal conductivity of $k_1 = 1.0\,\mathrm{W \cdot m^{-1} \cdot {}^{\circ}C^{-1}}$ and a diffusivity of $K_1 = 1.0 \times 10^4\,\mathrm{m^2 s^{-1}}$ (Medium 5 in Table I). The response is computed for two different inclusion materials that exhibit distinct thermal specific heats ($c_2 = 1.0 \times 10^{-4}\,\mathrm{J kg^{-1} \cdot {}^{\circ}C^{-1}}$ and $c_2 = 1.0 \times 10^{-2}\,\mathrm{J \cdot kg^{-1} \cdot {}^{\circ}C^{-1}}$) and a common thermal conductivity and density (Media 6 and 7 in Table I).

At $\tau = 0.0\,\mathrm{s}$, a source placed at ($x_s = 0.0\,\mathrm{m}$, $y_s = 0.0\,\mathrm{m}$) starts heating the solid medium at a constant rate with a unitary amplitude.

Copyright © 2010 John Wiley & Sons, Ltd.

DOI: 10.1002/nme

The calculations are performed in the frequency range $[0.0, 4096]$ Hz with a frequency increment of $\Delta\omega = 0.5$ Hz, and the imaginary part of the frequency is given by $\eta = 0.7\Delta\omega$. Figures 12(b) and (c) show the responses at $\tau = 1.0$ s using a temperature contour plot. The comparison of these plots with those provided by Gordeliy *et al.* [46] and by Furman and Neuman [47] indicates that the results are identical if one allows for the two misprints in Figure 5 of [47].

5. APPLICATIONS

The applicability of the proposed coupling formulations is illustrated by solving the case of a ring system filled with solid material, incorporating defects in its wall, similar to the geometry used to verify and evaluate the computational efficiency of the coupling algorithm (Section 3.2). This system is subjected to heat diffusion generated by a heat source placed in the inner medium. In the first set of examples, the thermal behavior of this system is addressed assuming the existence of an inclusion/defect with null thickness. The problem is solved assuming the existence of null heat fluxes along the boundary of the defect. The second set concerns the computation of the temperature field produced by the same heat source in the presence of a thin defect that is modeled as a solid-filled thin inclusion. The geometry of the ring, the material thermal properties of its wall (concrete), the solid filling the ring (steel) and the hosting fluid medium (air) are constant for all analyses. The thin defect is assumed to be filled with a thermal insulating material (polystyrene). The material properties of the different materials are as listed in Table I.

The computations are performed in the frequency domain for frequencies ranging from 0.0 to 0.01026 Hz, with a frequency increment of 0.2×10^{-4} Hz, which determines a total time window for the analysis of 13.89 h.

This system is subjected to a heat line source placed in the steel medium at point O(0.0 m, 0.0 m). The source time dependence is assumed to be parabolic. It starts emitting energy at instant $\tau \approx 1.0$ h and continues for 2.0 h (see Figure 13). The source's power is increased from 0.0 to 10 000.0 W, reaching maximum power at $\tau \approx 2.0$ h.

5.1. Null-thickness crack

The crack is placed in the middle of the ring's wall, forming a circular concentric arc of 45.0° with a radius of 0.4 m, as shown in Figure 9(a).

The crack is modeled imposing null heat flux along its surface. The null-thickness crack is discretized using 80 boundary elements. The inner and outer surfaces of the ring are modeled using a set of virtual heat sources placed at 0.015 m from the outer boundary and 0.009 m from inner boundary. The collocation points are evenly distributed along the wall surfaces. The inner and the outer interfaces of the ring were modeled using 240 and 400 virtual/collocation points, respectively.

The temperature distribution is obtained in a very fine two-dimensional grid of receivers. One thousand eight hundred twenty-one receivers were equally spaced along the inner solid, wall and outer hosting fluid.

A set of snapshots of the time evolution simulations is presented to illustrate the resulting heat diffusion across the ring wall. Figure 14 shows the temperature field in the vicinity of a null-thinness crack with null heat fluxes prescribed along its surface, at different time instants. To allow a better interpretation of the results, Figure 14 presents the logarithm of the temperature results.

Copyright © 2010 John Wiley & Sons, Ltd.

DOI: 10.1002/nme

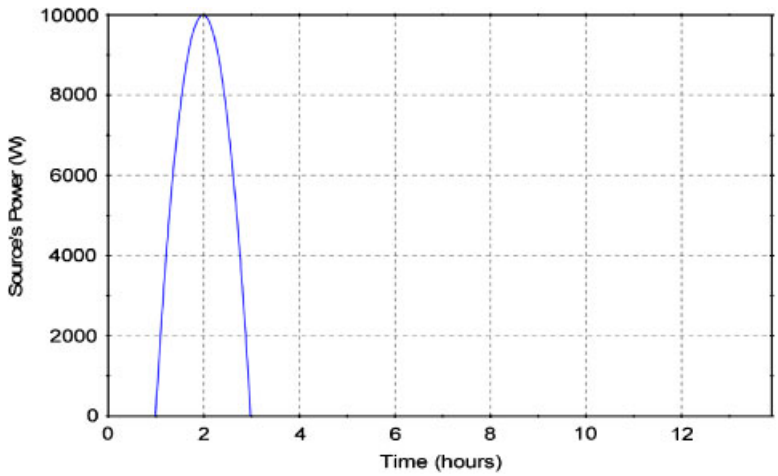

Figure 13. Heat source power time evolution.

A color scale is used in the plots, with the red and blue shades corresponding, respectively, to higher and lower values of temperature amplitudes. In the first plot, at $\tau \approx 1.46\,\text{h}$ (Figure 14(a)), after the heat source has started emitting energy, a circular heat field can be observed in the host medium caused by the energy propagation away from the heat source point. The incident heat pulse is visible propagating away from the source point without perturbations as it has not yet reached the wall of the ring. As expected, the amplitude of the temperature is uniform along the cylindrical heat wavefronts.

At $\tau \approx 4.18\,\text{h}$ (Figure 14(b)), the presence of the crack starts causing a perturbation of the heat transfer along the cross-section of the wall. As time passes, the heat spreads around the crack. However, the receivers placed in the ring's wall, behind the crack, register considerably lower temperatures than the receivers placed on the other side, as can be seen at time $\tau \approx 7.93\,\text{h}$ (Figure 14(c)). Although the source power has already dropped to 0.0 W at $\tau \approx 3.0\,\text{h}$, it is interesting to note that in the last snapshot, which was taken at $\tau \approx 13.89\,\text{h}$ (Figure 14(d)), the temperature is still rising in some regions of the domain. This means that the energy introduced at the source point continues to propagate to colder regions in order to establish the equilibrium condition.

5.2. Thin inclusion

In the second application, the temperature distribution is obtained when a thin inclusion is buried in the wall ring, and excited by a heat point source. The problem is analyzed using the coupling (TBEM+BEM)/MFS formulation. The thin inclusion is placed in the middle of the ring's wall, which is 0.02 m thick, forming a circular concentric arc of 45.0° with a radius of 0.4 m. The extremities of the thin inclusion are defined by semi-circumferences. As mentioned above, the thin inclusion is assumed to be filled with thermal insulating material. Figure 15 displays a cross-section of the problem. A part of the inclusion's surface is discretized by the TBEM formulation, whereas the rest is discretized by the BEM. This overcomes the difficulties posed by the BEM and by the

Copyright © 2010 John Wiley & Sons, Ltd.

DOI: 10.1002/nme

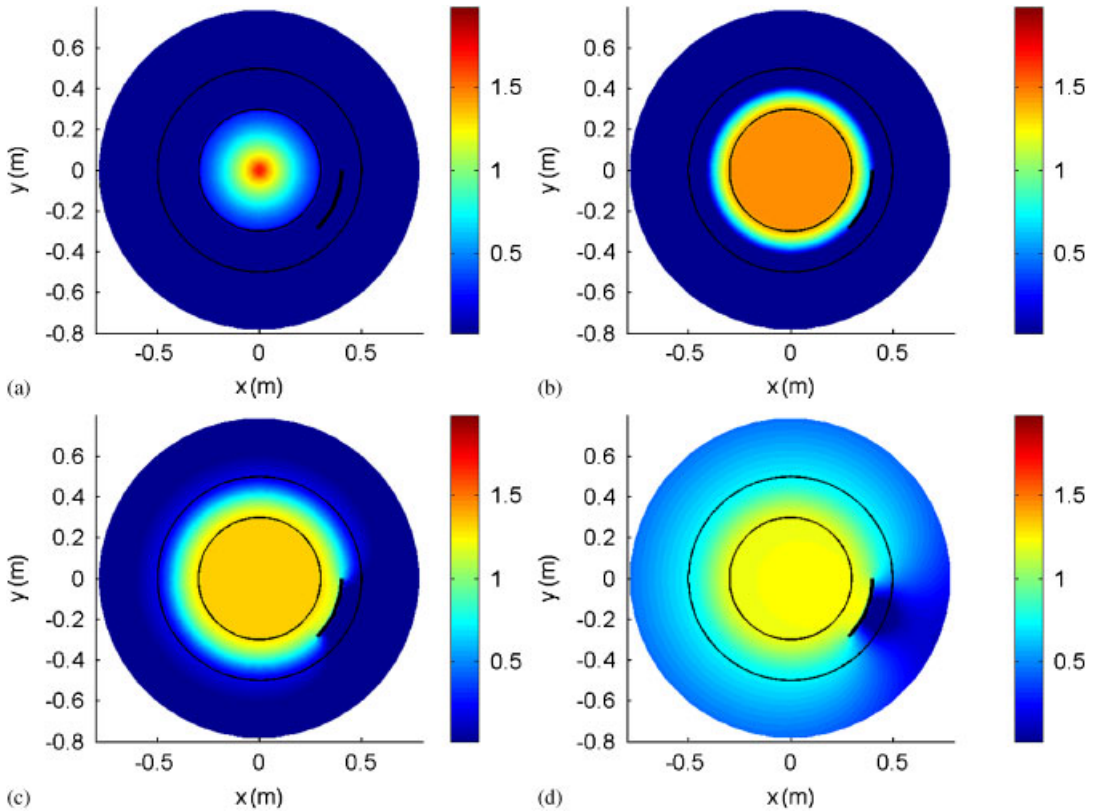

Figure 14. Temperature distribution (in °C) in the vicinity of a null-thickness crack, buried in a pipe wall, with null heat fluxes prescribed along its surface, heated by a cylindrical line source. Time responses at $\tau = 1.46\,\text{h}$ (a); $\tau = 4.18\,\text{h}$ (b); $\tau = 7.93\,\text{h}$ (c); and $\tau = 13.89\,\text{h}$ (d).

meshless technique when modeling thin inclusions. The inner and the outer surfaces of the ring are modeled using the MFS, which allows the use of a more efficient algorithm without loss of accuracy. The problem is solved assuming the continuity of temperatures and heat fluxes along all material interfaces.

The thin inclusion is discretized using 160 boundary elements. The inner and the outer surfaces of the ring are modeled using a set of virtual sources placed, as before, at a distance of 0.015 m from the outer boundary and 0.009 m from inner boundary. The inner and the outer interfaces of the ring were modeled, as before, with 240 and 400 virtual/collocation points, respectively.

Results were computed at the grid of receivers described above. The numerical results are presented in 2D views at different time instants (Figure 16), with logarithmic colored scale plots representing the total temperature field.

In the first plot, at time $\tau \approx 1.49\,\text{h}$ (Figure 16(a)), the temperature distribution is similar to that found before, in the presence of a empty crack, because the heat front has not yet reached the thin inclusion. When the heat front wave hits the thin inclusion filled with insulating material, only a

Copyright © 2010 John Wiley & Sons, Ltd.

DOI: 10.1002/nme

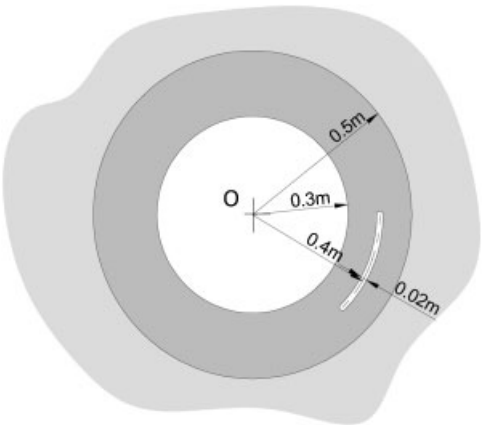

Figure 15. Geometry of a filled thin inclusion buried in a ring's wall and position of the source (O).

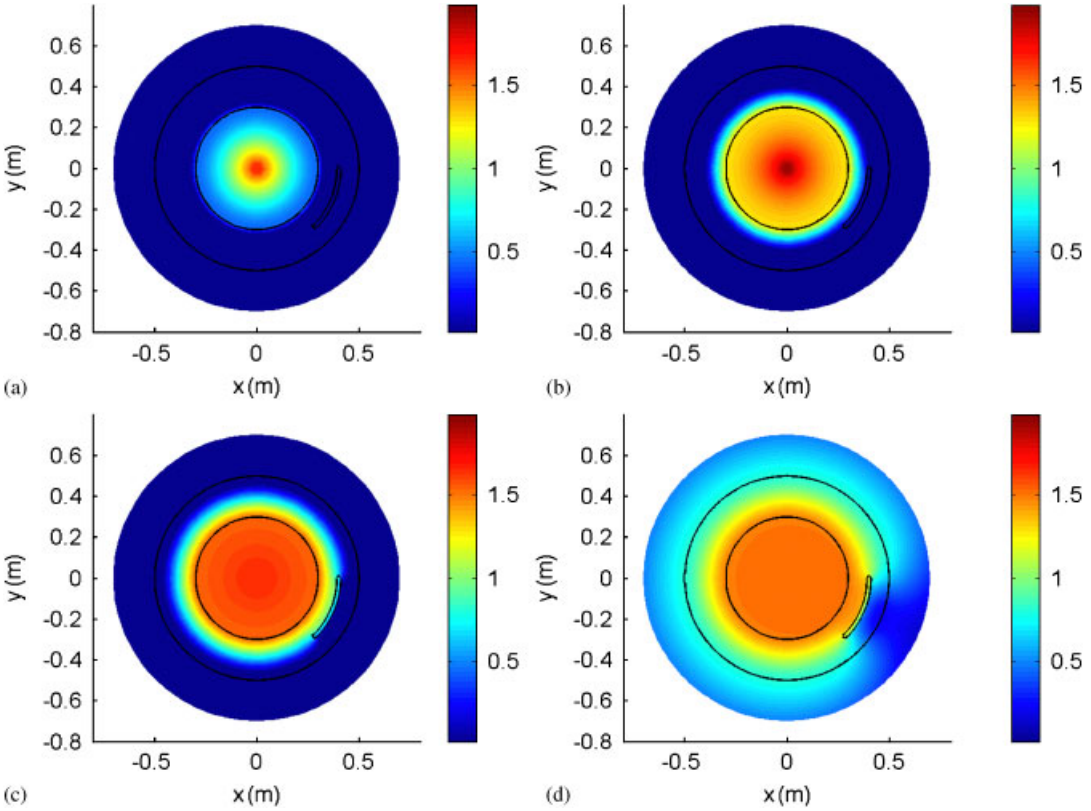

Figure 16. Temperature distribution (in °C) in the vicinity of a thin inclusion buried in a pipe wall, heated by a cylindrical line source. Time responses at $\tau = 1.49\,\mathrm{h}$ (a); $\tau = 2.22\,\mathrm{h}$ (b); $\tau = 3\,\mathrm{h}$ (c); and $\tau = 5.32\,\mathrm{h}$ (d).

Copyright © 2010 John Wiley & Sons, Ltd.

DOI: 10.1002/nme

very small perturbation is observed (see Figure 16(b)). At $\tau \approx 3.0\,\mathrm{h}$ (Figure 16(c)), the heat front component that passed through the thin inclusion has already reached the outer grid of receivers as it is propagating away from the source position. The propagation of heat reflected field and some diffraction patterns generated by the incident heat field at the extremities of the inclusion are clearly visible. By the last snapshot, taken at $\tau \approx 5.32\,\mathrm{h}$ (Figure 16(d)), the source power has already dropped to 0.0 W and it is interesting, as in the first example, to note that the temperature is still rising in some regions of the domain.

6. CONCLUSIONS

The coupling of the BEM/the TBEM and the MFS has been proposed for the transient analysis of heat diffusion. It was shown that the proposed coupling algorithms overcome the limitations posed by each method, allowing the use of less computational power but maintaining adequate accuracy.

The TBEM and a mixed formulation that uses both the TBEM and the classical BEM, coupled with the MFS, was proposed to overcome the thin-body difficulty. Problems involving thin heterogeneities, which can be empty or contain material, and other irregular inclusions, have been successfully addressed in this paper. The proposed coupling formulations were corroborated by comparing their solutions and analytical solutions, and they were seen to closely follow the behavior of the conventional direct BEM and TBEM formulations.

Finally, the proposed coupling formulations were applied to a set of numerical examples. The first example dealt with heat diffusion in the time domain across a solid-filled ring generated by a heat source, when an empty null-thickness crack is buried in the wall of a ring system. In the second set, the temperature distribution evolution across a solid-filled ring, in the presence of a thin inclusion that is filled with thermal insulating material, was computed to illustrate the capabilities of the proposed techniques.

APPENDIX A: ANALYTICAL SOLUTIONS FOR A CYLINDRICAL CIRCULAR RING CORE

Consider a ring defined by the internal and external radii, a and b, respectively, bounded by an exterior and interior medium, as illustrated in Figure A1. This ring is heated by a line harmonic source, placed in the exterior solid medium (with a thermal conductivity k_3, a density ρ_3, a specific heat c_3). The heat generated by this source propagates and hits the outer surface of the ring. After striking the outer surface of the cylindrical ring, part of the incident energy is reflected back into the exterior solid medium, and the remaining energy is transmitted into the ring material (with thermal conductivity k_1, density ρ_1, specific heat c_1), in the form of propagating energy. This energy continues to propagate and eventually strike the inner surface of the ring. There, a similar phenomenon may occur, with part of the energy being transmitted to the inner medium (with thermal conductivity k_2, density ρ_2, specific heat c_2) and the rest being reflected back to the ring medium. This process is repeated until all the energy is dissipated.

Copyright © 2010 John Wiley & Sons, Ltd.

DOI: 10.1002/nme

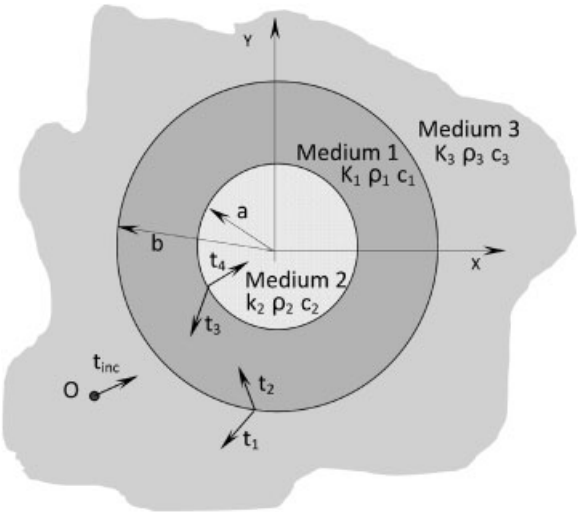

Figure A1. Circular ring core geometry.

A.1. Incident heat field (*or free-field*)

The incident field for a line harmonic heat source placed at $(x_0, 0)$ can be expressed by the following equation:

$$t_{\text{inc}}(r, \omega) = \frac{-\text{i}A}{4k_3} H_0(k_{\alpha_3} r_1) \tag{A1}$$

with $k_{\alpha_3} = \sqrt{-\text{i}\omega/K_3}$, $r_1 = \sqrt{(x-x_0)^2 + y^2}$. Equation (A1) expresses the incident field as heat terms centered at the source point $(x_0, 0)$, and not at the axis of the cylindrical inclusion, which constitutes a difficulty. In order to overcome this problem, the incident heat field can be expressed as heat terms centered at the origin. This is achieved by applying Graf's addition theorem [48], which results in the expressions below (in cylindrical coordinates):

$$\begin{aligned} t_{\text{inc}}(r, \omega, \theta) &= -\frac{\text{i}A}{4k_3} \sum_{n=0}^{\infty} (-1)^n \varepsilon_n J_n(k_{\alpha_3} r_0) H_n(k_{\alpha_3} r) \cos(n\theta) \quad \text{when } r > r_0 \\ t_{\text{inc}}(r, \omega, \theta) &= -\frac{\text{i}A}{4k_3} \sum_{n=0}^{\infty} (-1)^n \varepsilon_n H_n(k_{\alpha_3} r_0) J_n(k_{\alpha_3} r) \cos(n\theta) \quad \text{when } r < r_0 \end{aligned} \tag{A2}$$

in which r_0 is the distance from the source to the axis of the inclusion, $J_n(\ldots)$ are Bessel functions of order n, $\theta = \arctan(y/x)$ and

$$\varepsilon_n = \begin{cases} 1 & \text{if } n = 0 \\ 2 & \text{if } n \neq 0 \end{cases}$$

Copyright © 2010 John Wiley & Sons, Ltd.

DOI: 10.1002/nme

A.2. The scattered heat field in the outer medium

The heat generated in the exterior medium depends on heat coming from the external surface of the cylindrical ring, which propagates away from it. The outgoing heat can be defined using the following equation:

$$t_1(r,\omega,\theta)=\sum_{n=0}^{\infty} A_n H_n(k_{\alpha_3} r)\cos(n\theta) \tag{A3}$$

where A_n are unknown amplitudes.

A.3. The heat field in the ring

Two distinct groups of heat fields exist inside the ring, corresponding to heat generated at the external surface and traveling inwards, and to heat generated at the internal surface of the pipe that travels outwards. For the terms generated at the external boundary, the corresponding standing heat field is given by

$$t_2(r,\omega,\theta)=\sum_{n=0}^{\infty} B_n J_n(k_{\alpha_1} r)\cos(n\theta) \tag{A4}$$

where B_n are unknown amplitudes.

For the heat generated at the internal boundary, there is a corresponding diverging heat field, which can be defined by

$$t_3(r,\omega,\theta)=\sum_{n=0}^{\infty} C_n H_n(k_{\alpha_1} r)\cos(n\theta) \tag{A5}$$

where C_n are unknown amplitudes.

A.4. The heat field in the inner medium

In the inner medium (Medium 2), the heat field depends only on heat coming from the internal surface of the cylindrical ring core, and thus only inward propagating heat is generated. The corresponding heat field is

$$t_4(r,\omega,\theta)=\sum_{n=0}^{\infty} D_n J_n(k_{\alpha_2} r)\cos(n\theta) \tag{A6}$$

where $k_{\alpha_2}=\sqrt{-\mathrm{i}\omega/K_2}$ and D_n are unknown amplitudes.

A.5. Continuity of temperatures and normal heat fluxes on the two interfaces

The unknown coefficients A_n, B_n, C_n and D_n are determined by imposing the required boundary conditions. For the present case, the boundary conditions are the continuity of temperatures and normal heat fluxes on the two interfaces (see Figure A1). The four equations defined give rise to

Copyright © 2010 John Wiley & Sons, Ltd.

DOI: 10.1002/nme

a system of four equations with four unknowns, which yields the unknown coefficients.

$$\begin{aligned} t_{\text{inc}}(b,\omega,\theta)+t_1(b,\omega,\theta) &= t_2(b,\omega,\theta) \quad \text{at } r=b \\ k_3\frac{\partial[t_{\text{inc}}(b,\omega,\theta)+t_1(b,\omega,\theta)]}{\partial r} &= k_1\frac{\partial[t_2(b,\omega,\theta)]}{\partial r} \quad \text{at } r=b \\ t_2(a,\omega,\theta)+t_3(a,\omega,\theta) &= t_4(a,\omega,\theta) \quad \text{at } r=a \\ k_1\frac{\partial[t_2(a,\omega,\theta)+t_3(a,\omega,\theta)]}{\partial r} &= k_2\frac{\partial[t_4(a,\omega,\theta)]}{\partial r} \quad \text{at } r=a \end{aligned} \tag{A7}$$

Combining the above equations one obtains a system of equations, which is then used to find the unknown coefficients (A_n, B_n, C_n, D_n).

$$\begin{bmatrix} a_{11} & a_{12} & a_{13} & a_{14} \\ a_{21} & a_{22} & a_{23} & a_{24} \\ a_{31} & a_{32} & a_{33} & a_{34} \\ a_{41} & a_{42} & a_{43} & a_{44} \end{bmatrix} \begin{bmatrix} A_n \\ B_n \\ C_n \\ D_n \end{bmatrix} = (-1)^n \varepsilon_n \begin{bmatrix} b_1 \\ b_2 \\ b_3 \\ b_4 \end{bmatrix} \tag{A8}$$

with

$$\begin{aligned} a_{11} &= H_n(k_{\alpha_3}b), \quad a_{12} = -J_n(k_{\alpha_1}b), \quad a_{13} = -H_n(k_{\alpha_1}b), \quad a_{14} = 0 \\ a_{21} &= 0, \quad a_{22} = J_n(k_{\alpha_1}a), \quad a_{23} = H_n(k_{\alpha_1}a), \quad a_{24} = J_n(k_{\alpha_2}a) \\ a_{31} &= k_3[nH_n(k_{\alpha_3}b) - (k_{\alpha_3}b)H_{n+1}(k_{\alpha_3}b)] \\ a_{32} &= -k_1[nJ_n(k_{\alpha_1}b) - (k_{\alpha_1}b)J_{n+1}(k_{\alpha_1}b)] \\ a_{33} &= -k_1[nH_n(k_{\alpha_1}a) - (k_{\alpha_1}a)H_{n+1}(k_{\alpha_1}b)] \\ a_{34} &= 0 \\ a_{41} &= 0 \\ a_{42} &= k_1[nJ_n(k_{\alpha_1}a) - (k_{\alpha_1}a)J_{n+1}(k_{\alpha_1}a)] \\ a_{43} &= k_1[nH_n(k_{\alpha_1}a) - (k_{\alpha_1}a)H_{n+1}(k_{\alpha_1}a)] \\ a_{44} &= -k_2[nJ_n(k_{\alpha_2}a) - (k_{\alpha_2}a)J_{n+1}(k_{\alpha_2}a)] \\ b_1 &= \frac{\mathrm{i}A}{4k_3}H_n(k_{\alpha_3}r_0)J_n(k_{\alpha_3}b) \\ b_2 &= 0 \\ b_3 &= \frac{\mathrm{i}A}{4}H_n(k_{\alpha_3}r_0)[nJ_n(k_{\alpha_3}b) - (k_{\alpha_3}b)J_{n+1}(k_{\alpha_3}b)] \\ b_4 &= 0 \end{aligned}$$

Copyright © 2010 John Wiley & Sons, Ltd.

DOI: 10.1002/nme

Note that when the position of the heat source is changed, the terms a_{ij} of matrix remain the same, whereas the independent terms b_i are different. As the equations can be easily manipulated to consider another position for the source, they are not included here.

Null temperatures or null normal heat fluxes can be prescribed to the outer and the inner interfaces that lead to the simplification of the system defined above.

APPENDIX B: ANALYTICAL SOLUTIONS FOR A CIRCULAR CYLINDRICAL SYSTEM BURIED IN A HOMOGENEOUS UNBOUNDED FLUID MEDIUM, HOSTING TWO INCLUSIONS

Consider a circular cylindrical inclusion (Medium 1), centered at (x_1, y_1) with a radius a, hosting two circular solid inclusions (Media 2 and 4), centered at (x_2, y_2) and (x_3, y_3), with radii b and c, respectively. This system is bounded by an exterior medium (Medium 3), as illustrated in Figure B1(a). This system is heated by a harmonic line source, placed in the Medium 1 (x_0, y_0). The thermal conductivity, the density and the specific heat of each medium is defined by k_m, ρ_m, and c_m, where m is the number of media.

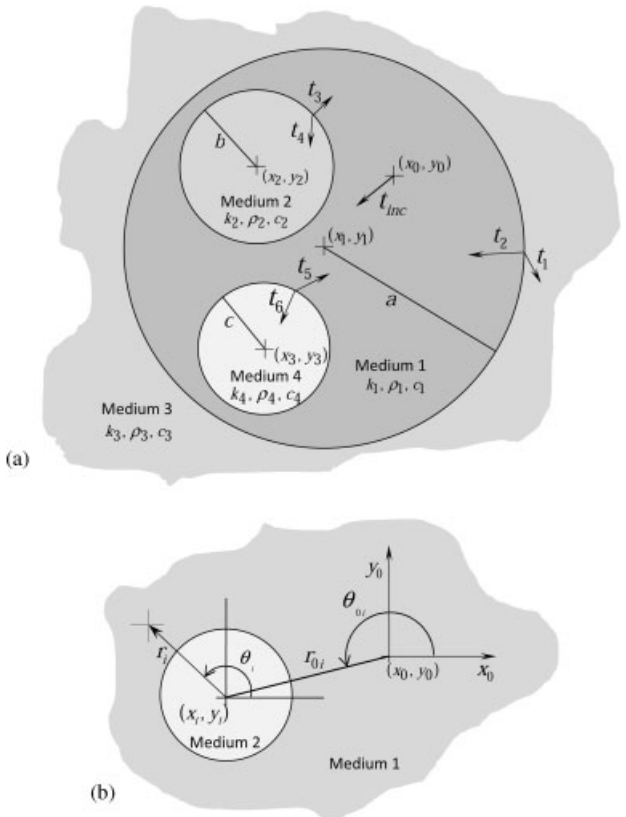

Figure B1. Non-concentric circular inclusions: (a) geometry of the problem and (b) Graf's addition theorem.

Copyright © 2010 John Wiley & Sons, Ltd.

DOI: 10.1002/nme

B.1. Incident heat field

The incident field can be expressed by

$$t_{\text{inc}}(r,\omega)=\frac{-\mathrm{i}A}{4k_1}H_0(k_{\alpha_1}r_0) \tag{B1}$$

with $k_{\alpha_1}=\sqrt{-\mathrm{i}\omega/K_1}$, $r_0=\sqrt{(x-x_0)^2+(y-y_0)^2}$. Equation (B1) expresses the incident field as heat terms centered at the source point (x_0, y_0), and not at the axes of the cylindrical inclusions. This is achieved by applying Graf's addition theorem [48], which results in the expressions below (in cylindrical coordinates):

$$\begin{aligned} t_{\text{inc}}(r,\omega,\theta) &= -\frac{\mathrm{iA}}{4k_1}\sum_{n=-\infty}^{\infty} J_n(k_{\alpha_1}r_{0i})H_n(k_{\alpha_1}r_i)(-1)^n\,\mathrm{e}^{\mathrm{i}n\theta_{0i}}\,\mathrm{e}^{\mathrm{i}n\theta_i} \quad \text{when } r_i>r_{0i} \\ t_{\text{inc}}(r,\omega,\theta) &= -\frac{\mathrm{iA}}{4k_1}\sum_{n=-\infty}^{\infty} H_n(k_{\alpha_1}r_{0i})J_n(k_{\alpha_1}r_i)(-1)^n\mathrm{e}^{\mathrm{i}n\theta_{0i}}\,\mathrm{e}^{\mathrm{i}n\theta_i} \quad \text{when } r_i<r_{0i} \end{aligned} \tag{B2}$$

in which r_{0i} is the distance from the source to the axis of the inclusions centered at (x_i, y_i), r_i is the distance from the point (x, y) to the inclusion centered at (x_i, y_i), $\theta_i=\arctan((y-y_i)/(x-x_i))$, $\theta_{0i}=\arctan((y_i-y_0)/(x_i-x_0))$ (see Figure B1(b)).

B.2. The scattered heat field in each cylindrical inclusion

In the inner medium of each inclusion, the heat field depends only on heat coming through its surface and thus only inwardly propagating heat is generated. In the outer medium, the heat is expressed by an outwardly propagating heat field.

- inclusion centered at (x_1, y_1)

$$t_1(r_1,\omega,\theta)=\sum_{n=-\infty}^{\infty} A_n H_n(k_{\alpha_3}r_1)\,\mathrm{e}^{\mathrm{i}n\theta_1} \tag{B3}$$

$$t_2(r_1,\omega,\theta)=\sum_{n=-\infty}^{\infty} B_n J_n(k_{\alpha_1}r_1)\,\mathrm{e}^{\mathrm{i}n\theta_1} \tag{B4}$$

- inclusion centered at (x_2, y_2)

$$t_3(r_2,\omega,\theta)=\sum_{n=-\infty}^{\infty} C_n H_n(k_{\alpha_1}r_2)\,\mathrm{e}^{\mathrm{i}n\theta_2} \tag{B5}$$

$$t_4(r_2,\omega,\theta)=\sum_{n=-\infty}^{\infty} D_n J_n(k_{\alpha_2}r_2)\,\mathrm{e}^{\mathrm{i}n\theta_2} \tag{B6}$$

- inclusion centered at (x_3, y_3)

$$t_5(r_3,\omega,\theta)=\sum_{n=-\infty}^{\infty} E_n H_n(k_{\alpha_1}r_3)\,\mathrm{e}^{\mathrm{i}n\theta_3} \tag{B7}$$

$$t_6(r_3,\omega,\theta)=\sum_{n=-\infty}^{\infty} F_n J_n(k_{\alpha_4}r_3)\,\mathrm{e}^{\mathrm{i}n\theta_3} \tag{B8}$$

where A_n, B_n, C_n, D_n, E_n and F_n are unknown amplitudes.

Copyright © 2010 John Wiley & Sons, Ltd.

DOI: 10.1002/nme

B.3. Continuity of temperatures and normal heat fluxes at the two interfaces

The unknown coefficients are computed by imposing the continuity of normal heat fluxes and temperatures at the three interfaces (see Figure B1(a)).

$$k_3\frac{\partial[t_1(a,\omega,\theta)]}{\partial r_1}=k_1\left[\frac{\partial[t_2(a,\omega,\theta)+t_3(a,\omega,\theta)+t_5(a,\omega,\theta)+t_{\mathrm{inc}}(a,\omega,\theta)]}{\partial r_1}\right]\quad \text{at } r_1=a$$

$$t_1(a,\omega,\theta)=t_2(a,\omega,\theta)+t_3(a,\omega,\theta)+t_5(a,\omega,\theta)+t_{\mathrm{inc}}(a,\omega,\theta)\quad \text{at } r_1=a \tag{B9}$$

$$k_2\frac{\partial[t_4(b,\omega,\theta)]}{\partial r_2}=k_1\left[\frac{\partial[t_2(b,\omega,\theta)+t_3(b,\omega,\theta)+t_5(b,\omega,\theta)+t_{\mathrm{inc}}(b,\omega,\theta)]}{\partial r_2}\right]\quad \text{at } r_2=b$$

$$t_4(b,\omega,\theta)=t_2(b,\omega,\theta)+t_3(b,\omega,\theta)+t_5(b,\omega,\theta)+t_{\mathrm{inc}}(b,\omega,\theta)\quad \text{at } r_2=b \tag{B10}$$

$$k_4\frac{\partial[t_6(c,\omega,\theta)]}{\partial r_3}=k_1\left[\frac{\partial[t_2(c,\omega,\theta)+t_3(c,\omega,\theta)+t_5(c,\omega,\theta)+t_{\mathrm{inc}}(c,\omega,\theta)]}{\partial r_3}\right]\quad \text{at } r_3=c$$

$$t_6(c,\omega,\theta)=t_2(c,\omega,\theta)+t_3(c,\omega,\theta)+t_5(c,\omega,\theta)+t_{\mathrm{inc}}(c,\omega,\theta)\quad \text{at } r_3=c \tag{B11}$$

Equation (B9) requires that $t_3(r_2,\omega,\theta)$ and $t_5(r_3,\omega,\theta)$ are expressed as heat terms centered at the axis of (x_1, y_1); $t_2(r_1,\omega,\theta)$ and $t_5(r_3,\omega,\theta)$ are written as heat terms centered at the axis of (x_2, y_2); $t_2(r_1,\omega,\theta)$ and $t_3(r_2,\omega,\theta)$ are written as heat terms centered at the axis of (x_3, y_3). This is achieved, as before, by applying Graf's addition theorem, which leads to the following expressions:

$$t_2(r_i,\omega,\theta)=\sum_{n=-\infty}^{\infty}B_n\sum_{m=-\infty}^{\infty}J_{n+m}(k_{\alpha_1}r_{1i})J_m(k_{\alpha_1}r_i)(-1)^m\,\mathrm{e}^{\mathrm{i}(m+n)\theta_{1i}}\,\mathrm{e}^{-\mathrm{i}m\theta_i} \tag{B12}$$

$$t_3(r_i,\omega,\theta)=\sum_{n=-\infty}^{\infty}C_n\sum_{m=-\infty}^{\infty}H_{n+m}(k_{\alpha_1}r_{2i})J_m(k_{\alpha_1}r_i)(-1)^m\,\mathrm{e}^{\mathrm{i}(m+n)\theta_{2i}}\,\mathrm{e}^{-\mathrm{i}m\theta_i} \tag{B13}$$

$$t_5(r_i,\omega,\theta)=\sum_{n=-\infty}^{\infty}E_n\sum_{m=-\infty}^{\infty}H_{n+m}(k_{\alpha_1}r_{3i})J_n(k_{\alpha_1}r_i)(-1)^m\,\mathrm{e}^{\mathrm{i}(m+n)\theta_{3i}}\,\mathrm{e}^{-\mathrm{i}m\theta_i} \tag{B14}$$

where r_{ji} $(j=1,2,3)$ is the distance from the center of the inclusions (x_j, y_j) to the axis of the inclusions centered at (x_i, y_i), r_i is the distance from the point (x, y) to the axis of each inclusion, $\theta_i=\arctan((y-y_i)/(x-x_i))$, $\theta_{ji}=\arctan((y_i-y_j)/(x_i-x_j))$ (see Figure B1(b)).

Combining the above equations, one obtains a system of equations that is then used to find the unknown coefficients (A_n, B_n, C_n, D_n, E_n and F_n). However, it is not possible to define, as it was in the case of circular concentric inclusions, a linear system of equations for each value of n. In this case, the full set of unknowns is defined in a unique system of equations that requires the maximum values of n and m to be predefined.

Null temperatures or null normal heat fluxes can be prescribed at the inclusions' surfaces, which allow the simplification of the above system of equations.

Copyright © 2010 John Wiley & Sons, Ltd.

DOI: 10.1002/nme

ACKNOWLEDGEMENTS

The research work presented herein was supported by the Portuguese Foundation for Science and Technology (FCT), under research project SFRH/BD/48138/2008.

REFERENCES

1. Jokisalo J, Kurnitski J, Korpi M, Kalamees T, Vinha J. Building leakage, infiltration, and energy performance analyses for Finnish detached houses. *Building and Environment* 2009; **44**:377–387. DOI: 10.1016/j.buildenv.2008.03.014.
2. Poblete A, Acebes Pascual M. Thermographic measurement of the effect of humidity in mortar porosity. *Infrared Physics and Technology* 2007; **49**:224–227. DOI: 10.1016/j.infrared.2006.06.009.
3. Sham FC, Chen N, Long L. Surface crack detection by flash thermography on concrete surface. *Insight* 2008; **50**(5):240–243. DOI: 10.1784/insi.2008.50.5.240.
4. Maierhofer Ch, Arndt R, Röllig M. Influence of concrete properties on the detection of voids with impulse-thermography. *Infrared Physics and Technology* 2007; **49**:213–217. DOI: 10.1016/j.infrared.2006.06.007.
5. Chenga C, Chenga T, Chiang C. Defect detection of concrete structures using both infrared thermography and elastic waves. *Automation in Construction* 2008; **18**(1):87–92. DOI: 10.1016/j.autcon.2008.05.004.
6. Chang YP, Kang CS, Chen DJ. The use of fundamental Green functions for solution of problems of heat conduction in anisotropic media. *International Journal of Heat and Mass Transfer* 1973; **16**:1905–1918.
7. Bialecki RA, Jurgas P, Kuhn G. Dual reciprocity BEM without matrix inversion for transient heat conduction. *Engineering Analysis with Boundary Elements* 2002; **26**(3):227–236.
8. Wrobel LC, Brebbia CA. A formulation of the boundary element method for axisymmetric transient heat conduction. *International Journal of Heat and Mass Transfer* 1981; **24**:843–850. DOI: 10.1016/S0017-9310(81)80007-5.
9. Dargush GF, Banerjee PK. Application of the boundary element method to transient heat conduction. *International Journal for Numerical Methods in Engineering* 1991; **31**:1231–1247.
10. Lesnic D, Elliot L, Ingham DB. Treatment of singularities in time-dependent problems using the boundary element method. *Engineering Analysis with Boundary Elements—EABE* 1995; **16**:65–70. DOI: 10.1016/0955-7997(95)00065-8.
11. Rizzo FJ, Shippy DJ. A method of solution for certain problems of transient heat conduction. *AIAA Journal* 1970; **8**:2004–2009.
12. Cheng AHD, Abousleiman Y, Badmus T. A Laplace transform BEM for axisymmetric diffusion utilizing pre-tabulated Green's function. *Engineering Analysis with Boundary Elements* 1992; **9**:39–46.
13. Zhu SP, Satravaha P, Lu X. Solving the linear diffusion equations with the dual reciprocity methods in Laplace space. *Engineering Analysis with Boundary Elements* 1994; **13**:1–10.
14. Zhu SP, Satravaha P. An efficient computational method for modeling transient heat conduction with nonlinear source terms. *Applied Mathematical Modeling* 1996; **20**(7):513–522. DOI: 10.1016/0307-904X(95)00170-O.
15. Sutradhar A, Paulino GH, Gray LJ. Transient heat conduction in homogeneous and non-homogeneous materials by the Laplace transform Galerkin boundary element method. *Engineering Analysis with Boundary Elements* 2002; **26**(2):119–132.
16. Stehfest H. Algorithm 368: numerical inversion of Laplace transform. *Communications of the Association for Computing Machinery* 1970; **13**(1):47–49.
17. Papoulis A. A new method of inversion of the Laplace transform. *Quarterly of Applied Mathematics* 1957; **14**:405–414.
18. Simões N, Tadeu A. Transient conduction and convection heat transfer across a multi-layer floor subjected to multiple heat sources. *Building and Environment* 2006; **41**(10):1299–1310. DOI: 10.1016/j.buildenv.2005.05.012.
19. Tadeu A, Simões N. Three-dimensional fundamental solutions for transient heat transfer by conduction in an unbounded Medium, half-space, slab and layered media. *Engineering Analysis with Boundary Elements* 2006; **30**(5):338–349. DOI: 10.1016/j.enganabound.2006.01.011.
20. Simões N, Tadeu A. Fundamental solutions for transient heat transfer by conduction and convection in an unbounded, half-space, slab and layered media in the frequency domain. *Engineering Analysis with Boundary Elements* 2005; **29**(12):1130–1142. DOI: 10.1016/j.enganabound.2005.06.002.
21. Joanni AE, Kausel E. Heat diffusion in layered media via the thin-layer method. *International Journal for Numerical Methods in Engineering* 2009; **78**(6):692–712.

Copyright © 2010 John Wiley & Sons, Ltd.

22. Starnes MA. Development of technical bases for using infrared thermography for nondestructive evaluation of fiber reinforced polymer composites bonded to concrete. *Dissertation*, submitted to the Department of Civil Engineering at the Massachusetts Institute of Technology (MIT) in partial fulfillment of the requirements for the degree of Doctor of Philosophy, Cambridge, MA, 2002.
23. Hohage T, Sayas FJ. Numerical solution of a heat diffusion problem by boundary element methods using the Laplace transform. *Numerische Mathematik* 2005; **102**:67–92. DOI: 10.1007/s00211-005-064-y.
24. Ma F, Chatterjee J, Henry DP, Banerjee PK. Transient heat conduction analysis of 3D solids with fiber inclusions using the boundary element method. *International Journal for Numerical Methods in Engineering* 2008; **73**: 1113–1136.
25. Wang CH, Grigoriev MM, Dargush GF. A fast multi-level convolution boundary element method for transient diffusion problems. *International Journal for Numerical Methods in Engineering* 2005; **62**:1895–1926.
26. Dell'erba DN, Aliabadi MH, Rooke DP. Dual boundary element method for three-dimensional thermoelastic crack problems. *International Journal of Fracture* 1998; **94**:89–101.
27. Prosper D. Modeling and detection of delaminations in laminated plates. *Ph.D. Thesis*, MIT, Cambridge, 2001.
28. Prosper D, Kausel E. Wave scattering by cracks in laminated media. In *Proceedings of the International Conference on Computational Engineering and Science ICES'01*, Puerto Vallarta 2001, Mexico, Atluri SN, Nishioka T, Kikuchi M (eds). Tech Science Press, 19–25 August 2001.
29. Rudolphi TJ. The use of simple solutions in the regularisation of hypersingular boundary integral equations. *Mathematical and Computer Modelling* 1991; **15**:269–278.
30. Lutz E, Ingraffea AR, Gray LJ. Use of 'simple solutions' for boundary integral methods in elasticity and fracture analysis. *International Journal for Numerical Methods in Engineering* 1992; **35**:1737–1751.
31. Amado Mendes P, Tadeu A. Wave propagation in the presence of empty cracks in an elastic Medium. *Computational Mechanics* 2006; **38**(3):183–199. (Published online 2/Sept/2005), DOI: 10.1007/s00466-005-0737-7.
32. Tadeu A, Amado Mendes P, António J. 3D elastic wave propagation modelling in the presence of 2D fluid filled thin inclusions. *Engineering Analysis with Boundary Elements* (Special Issue 'Non-Traditional Boundary Integral Formulations, Part II') 2006; **30**(3):176–193. DOI: 10.1016/j.enganabound.2005.08.014.
33. Fairweather G, Karageorghis A. The method of fundamental solutions for elliptic boundary value problems. *Advances in Computational Mathematics* 1998; **9**:69–95.
34. Fairweather G, Karageorghis A, Martin PA. The method of fundamental solutions for scattering and radiation problems. *Engineering Analysis with Boundary Elements* 2003; **27**:759–769. DOI: 10.1016/S0955-7997(03)00017-1.
35. Chen JT, Chang MH, Chen KH, Chen IL. Boundary collocation method for acoustic eigenanalysis of three-dimensional cavities using radial basis function. *Computational Mechanics* 2002; **29**:392–408.
36. Song K, Zhang X, Lu M. Meshless method based on collocation with consistent compactly supported radial basis functions. *Acta Mechanica Sinica* 2004; **20**(5):551–557.
37. Smyrlis YS. The method of fundamental solutions: a weighted leastsquares approach. *BIT* 2006; **46**:163–194.
38. Brown D, Ling L, Kansa E, Levesley J. On approximate cardinal preconditioning methods for solving PDEs with radial basis functions. *Engineering Analysis with Boundary Elements* 2005; **29**:343–353. DOI: 10.1016/j.enganabound.2004.05.006.
39. Godinho L, Tadeu A, Simões N. Accuracy of the MFS and BEM on the analysis of acoustic wave propagation and heat conduction problems. In *Advances in Meshless Methods*, Jan S, Vladimir S (eds). Tech Science Press, 2006.
40. Godinho L, Tadeu A, Amado Mendes P. Wave propagation around thin structures using the MFS. *Computers, Materials, and Continua* 2007; **5**:117–128.
41. Godinho L, Amado Mendes P, Tadeu A, Cadena-Isaza A, Smerzini C, Sánchez-Sesma FJ, Madec R, Komatitsch D. Numerical simulation of ground rotations along 2D topographical profiles under the incidence of elastic plane waves. *Bulletin of the Seismological Society of America* 2009; **99**(2B):1147–1161. DOI: 10.1785/0120080096.
42. Alves CJS, Leitão VMA. Crack analysis using an enriched MFS domain decomposition technique. *Engineering Analysis with Boundary Elements* 2006; **30**(3):160–610. DOI: 10.1016/j.enganabound.2005.08.012.
43. Manolis GD, Beskos DE. *Boundary Element Methods in Elastodynamics*, Unwin Hyman (sold to Chapman and Hall): London, 1988.
44. Tadeu AJB, Santos PFA, Kausel E. Closed-form integration of singular terms for constant, linear and quadratic boundary elements. Part I. SH wave propagation. *Engineering Analysis with Boundary Elements* 1999; **23**(8): 671–681. DOI: 10.1016/S0955-7997(99)00016-8.

Copyright © 2010 John Wiley & Sons, Ltd.

45. Guiggiani M. Formulation and numerical treatment of boundary integral equations with hypersingular kernels. *Singular Integrals in Boundary Element Methods*. Computational Mechanics Publications: Southampton (U.K.), Boston (U.S.A.), 2006.
46. Gordeliy E, Mogilevskaya SG, Crouch SL. Transient heat conduction in a medium with multiple circular cavities and inhomogeneities. *International Journal for Numerical Methods in Engineering* 2010; **80**(11):1437–1462. DOI: 10.1002/nme.2671.
47. Furman A, Neuman SP. Laplace-transform analytic element solution of transient flow in porous media. *Advances in Water Resources* 2003; **26**:1229–1237.
48. Watson GN. *A Treatise on the Theory of Bessel Functions* (2nd edn). Cambridge University Press: Cambridge, 1980.

Copyright © 2010 John Wiley & Sons, Ltd.